

Measurement of the associated production of a Z boson and bottom or charm quarks with the ATLAS experiment

Jacob Oliver

February 10, 2021

Abstract

This document presents the first step in obtaining unfolded cross sections of the $Z \rightarrow (\ell\ell) + b$ and $Z \rightarrow (\ell\ell) + b\bar{b}$ channels with $\ell\ell$ corresponding to a muon or electron pair, in addition to measurements of kinematic variables. The analysis uses data collected by the ATLAS experiment at the LHC of p-p collisions corresponding to 139fb^{-1} at a centre of mass energy of $\sqrt{s} = 13\text{ TeV}$. The benefits of a measurement of unfolded cross sections of kinematic variables for these processes are briefly discussed before the presentation of the measurement results. The plots show a good modelling of data by the Monte Carlo simulation, and provide an adequate starting point for later analysis and unfolding of these cross sections.

Contents

1	Introduction	1
2	Physical Theory	3
2.1	The Standard Model	3
2.2	Describing the Standard Model Mathematically	6
2.2.1	Quantum Chromodynamics	6
2.2.2	Electroweak Theory	7
2.2.3	Higgs Mechanism	8
2.3	Signal Processes	11
2.4	Background Processes	12
3	LHC and ATLAS	16
3.1	LHC	16
3.1.1	Acceleration at the LHC	16
3.1.2	Beam Structure	19
3.1.3	Luminosity	20
3.1.4	Pileup	22
3.2	ATLAS	23
3.2.1	The ATLAS Coordinate System	24
3.2.2	The Magnet System	25
3.2.3	The Inner Detector	26
3.2.4	The Calorimeters	30
3.2.5	The Muon Spectrometer	34
3.3	ATLAS	37
3.3.1	Magnet System	38
3.3.2	Inner Detector	39
3.3.3	Calorimeter System	40
3.3.4	Muon System	43
3.3.5	Trigger System	45

1 Introduction

The production of a Z boson from p-p collisions is an ideal target for analysis due to the strong identifiers of the process. The clear experimental signature of a Z boson decaying to a lepton pair is combined with the long lifetimes of b-hadrons to create a signature which is easy to observe, and that provides an excellent opportunity to study the production and dynamics of heavy flavour physics (heavy flavour physics is physics pertaining to quarks at the heavier end of the scale, namely bottom and charm, but not top quarks which have their own area of study).

In the Standard Model (SM), there are multiple processes which create the signal source of Z boson production in association with two b quarks, with the Z boson later decaying to two leptons. While these processes occur via different mechanisms, they all arrive at the same final state which this analysis examines. The Z boson production is only possible through the electroweak interaction, however strong interactions also take place in each of the signal processes. The most common of these processes occurs via the radiation of a gluon which splits into a bb pair. This is one of the central motivations to measuring $Z \rightarrow (\ell\ell) + bb$ processes: performing a measurement of the strong signal processes allows the investigation of QCD phenomena and strong coupling coefficients, which could potentially lead to a more precise SM in the future.

Current $Z \rightarrow (\ell\ell) + bb$ cross sections are calculated using next-to-leading-order perturbative quantum chromodynamics (NLO pQCD), and are associated with large theoretical uncertainties [1]. Cross sections of $Z \rightarrow (\ell\ell) + bb$ interactions have been available for some time [2–4]. These processes have already been measured at lower centre of mass energy by both ATLAS [5] and CMS [6], however performing a more current analysis allows for several improvements over previous studies. Key among these improvements is access to the full dataset produced by ATLAS during Run2, which allows the analysis to be extended to phase spaces with lower cross sections.

Currently NLO pQCD calculation involving heavy flavour are associated with one of two schemes named the four-flavour number scheme (4FNS) and five-flavour number scheme (5FNS). In the 4FNS b quarks do not contribute to the proton wave-function and are considered to be massive (i.e. only the parton densities of gluons and the first two quark generations are considered within the proton). In the 5FNS, the b quark is treated as massless and the presence of an additional b quark density is assumed within the proton [7].

By definition these schemes must always give identical results if contributions from all orders are added, however the manner of ordering the perturbative expansion is not consistent between the two schemes at any given order. This allows the possibility of a difference between the two schemes to arise, however this can only occur when the schemes are considered at a fixed order. There are advantages and disadvantages to each of the schemes [8], and this analysis allows an insight into both the 4FNS and 5FNS.

The $Z \rightarrow (\ell\ell) + b$ process is a useful tool for probing the structure of the proton, due to the presence of the additional b quark density in the initial state of the proton prior to collision (as described by the 5FNS). The $Z \rightarrow (\ell\ell) + b$ is sensitive to this b quark density and measurements of its production could constrain the b quark parton density function (PDF)[9] of the proton.

Another benefit of performing a measurement of this process comes when considering its relation to other physical processes. The final state of a lepton pair and two b quarks is not uncommon, and many other processes have similar final states which leads to $Z \rightarrow (\ell\ell) + bb$ being a common background. Many processes across multiple physical areas share this background, such as Higgs processes, and Dark Matter and SUSY searches. By obtaining a detailed measurement of $Z \rightarrow (\ell\ell) + bb$ production, it is possible to improve the precision of many searches with similar final states.

There are, however, difficulties in performing a measurement such as this. Just as $Z \rightarrow (\ell\ell) + bb$ provides a background for many physical searches due to the shared final state, there are many additional background processes to $Z \rightarrow (\ell\ell) + bb$. This makes a direct measurement difficult; an informed understanding of the background processes involved is essential in order to perform a good measurement.

The following report outlines and explains the steps used to perform a measurement of these processes using data collected by ATLAS at the LHC.

2 Physical Theory

2.1 The Standard Model

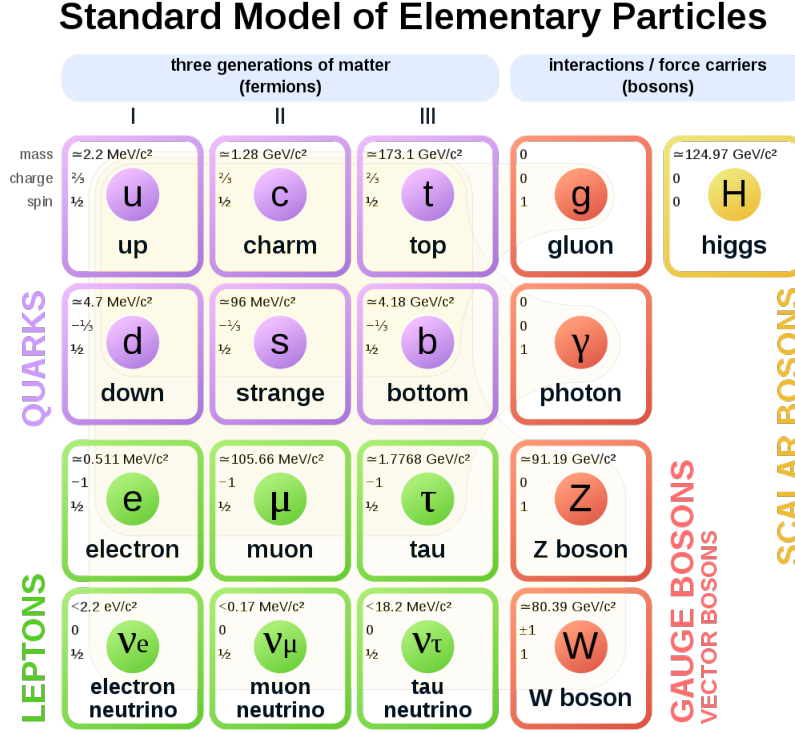


Figure 2.1: The Standard Model of particle physics.

To study particle physics is to study the fundamental constituents of matter, and the interactions between them. In order to describe both these constituents and the interactions between them, a model called the Standard Model (SM) is used. The SM is a local, Lorentz-invariant quantum field theory. These interactions arise from the requirement of local gauge invariance within the SM, and can be described by group theory. The SM gauge group is as follows:

$$SU(3)_C \otimes SU(2)_L \otimes U(1)_Y \quad (1)$$

where C is colour, L is left-handedness, and Y is hypercharge. In the SM, constituent matter particles are titled *fermions*: half integer spin particles that obey Fermi Dirac statistics. The forces that cause the interactions between fermions are described by

Gauge Boson	Mass	Charge	Spin	Force	Theory
gluon	0	0	1	strong	QCD
W^\pm	80.379 ± 0.012	± 1	1	weak	Electroweak
Z^0	91.1876 ± 0.0021	0	1	weak	Electroweak
γ	$< 1 \times 10^{-18}$	0	1	electromagnetic	Electroweak

Table 2.1: A table showing the properties of the Standard Model gauge bosons[7].

gauge bosons: integer spin particles that obey Bose Einstein statistics. Each force is carried by a particular type of these mediator bosons: photons (γ) carry the electromagnetic force, gluons (g) carry the strong force, and W^\pm and Z^0 bosons carry the weak force. Gravity is the only known fundamental force that is not described by the SM. Table 2.1 summarises the properties of the SM bosons.

Fermions can be further subsectioned into two separate groups: quarks and leptons. Each group has three generations which, as a general rule of thumb, have increasing particle mass from generation to generation.

Leptons are classified by their charge (Q), lepton flavour number (the lepton flavour number is different for each generation of lepton and can be electron number (L_e), muon number (L_μ), or tau number (L_τ)), and the third component of weak isospin (T_3). It is also important to consider the additional quantity of weak hypercharge (Y_W) which is directly related to both the lepton charge and weak isospin by the equation:

$$Y_W = 2 \cdot (Q - T_3) \quad (2)$$

The charged leptons (i.e. e , μ , and τ) are able to interact via both the weak and the electromagnetic force, however the neutral leptons (ν_e , ν_μ , and ν_τ) can only interact with the weak force. Table 2.2 summarises the properties of leptons within the SM.

For each lepton a left-handed weak isospin doublet is formed:

$$\begin{pmatrix} T_3 = +1/2 \\ T_3 = -1/2 \end{pmatrix} = \begin{pmatrix} \nu_{eL} \\ e_L^- \end{pmatrix}, \begin{pmatrix} \nu_{\mu L} \\ \mu_L^- \end{pmatrix}, \begin{pmatrix} \nu_{\tau L} \\ \tau_L^- \end{pmatrix} \quad (3)$$

The SM forbids right-handed neutrinos, and as such weak isospin singlets ($T_3 = 0$) are formed by the right handed leptons in each generation: e_R^- , μ_R^- , and τ_R^- .

Quarks are classified by their charge (Q), and their flavour quantum numbers: baryon number (the third component of the isospin (I_3)), strangeness (S), charmness (C), bottomness (B), and topness (T). Unlike the SM bosons and leptons, quarks are able to

Lepton Flavour	Mass	Q	Y_W	L_e	L_μ	L_τ
e^-	0.511 MeV	-1	-1	1	0	0
ν_e	< 2 eV	0	-1	1	0	0
μ	105.7 MeV	-1	-1	0	1	0
ν_μ	< 0.19 MeV	0	-1	0	1	0
τ	1776.8 MeV	-1	-1	0	0	1
ν_τ	< 18.2 MeV	-1	-1	0	0	1

Table 2.2: A table showing the properties of the Standard Model leptons[7].

Quark Flavour	Mass	Q	I_3	C	S	T	B
u	$2.3^{+0.7}_{-0.5}$ MeV	2/3	1/2	0	0	0	0
d	$4.8^{+0.7}_{-0.3}$ MeV	-1/3	-1/2	0	0	0	0
c	1.275 ± 0.025 GeV	2/3	0	1	0	0	0
s	95 ± 5 MeV	-1/3	0	0	-1	0	0
t	173.2 ± 0.9 GeV	2/3	0	0	0	1	0
b	4.18 ± 0.03 GeV	-1/3	0	0	0	0	-1

Table 2.3: A table showing the properties and quantum numbers of the SM quarks[7].

interact via all three of the fundamental forces. In addition to these flavour quantum numbers, quarks also have an additional quantum number named colour charge which can take one of three values (often referred to as red, blue, or green). The term colour only describes this quantum numbers, and not the colour of visible light. Table 2.3 summarises the properties of the SM quarks.

In addition to the quarks and leptons, each fermion has its own antiparticle. These antiparticles are opposites to their matter particles, with reversed signs for all quantum numbers. We can obtain the total number of fermions in the standard model by simply summing their number: 6 leptons, 6 anti-leptons, 18 quarks (there are three variations for each quark flavour due to the three colour charges), and 18 antiquarks. This gives the SM a total of 12 leptons and 36 quarks.

The SM is a highly successful model and the predictions of the models have been tested to very high levels of accuracy by CERN, however it is known that the model is imperfect (hence the need for experimental physics). In order to improve the model, it must be rigorously tested in every facet until it is broken (such that it can then be revised and improved).

An example of this process can be seen by considering the constraint placed on the SM by electroweak (EW) theory: under EW theory, the masses of the W^\pm and Z^0 bosons

(i.e. the gauge bosons of the weak force) violate invariance under local gauge transformations. However, despite this the W^\pm and Z^0 bosons have large masses. In order to account for this within the SM, the Higgs mechanism is required. The Higgs mechanism results in the presence of an additional gauge boson with a mass of 125 GeV in the SM known as the Higgs boson [10][11]. The Higgs mechanism is described in greater detail in section 2.2.3.

2.2 Describing the Standard Model Mathematically

2.2.1 Quantum Chromodynamics

The strong interaction is described by a process known as Quantum Chromodynamics (QCD)[7][12]: a non-Abelian gauge theory based on the $SU(3)$ symmetry group of colour. This group has eight generators which correspond to the eight massless gluons that mediate the interactions of coloured quarks. These quarks are described by colour triplets:

$$q_f^T = (q_f^1, q_f^2, q_f^3) \quad (4)$$

with 1, 2, and 3 representing the three colour states of red, green, and blue. The Lagrangian density of QCD is given by

$$L_{QCD} = \sum_{j=1}^{n_f} \bar{q}_j (iD_\mu \gamma^\mu - m_j) q_j - \frac{1}{4} \sum_{A=1}^8 F^{A\mu\nu} F_{\mu\nu}^A \quad (5)$$

The first sum of this equation corresponds to the quark contribution, and the second the gluon contribution. This equation is written with the quark-field spinors, q_j , and the quark masses m_j . $D_\mu = \partial_\mu - ig_s T_A \mathcal{A}_\mu^A$ is the covariant derivative, where \mathcal{A}_μ^A correspond to the gluon fields and T_A to the eight generators of the $SU(3)$ symmetry group. The γ^μ represent the Dirac matrices and $F_{\mu\nu}^A$ represents the field strength tensor based on the gluon field \mathcal{A}_μ^A

$$F_{\mu\nu}^A = \partial_\mu \mathcal{A}_\nu^A - \partial_\nu \mathcal{A}_\mu^A - g_s f_{ABC} \mathcal{A}_\mu^B \mathcal{A}_\nu^C \quad (6)$$

with the QCD coupling constant, $g_s = \sqrt{4\pi\alpha_s}$, and the structure constants of the SU(3) symmetry group.

The SU(3) group is a non-Abelian group and as such the third term in Eq. 6 does not vanish and thus the present gluon fields are able to self-interact. The self interaction leads to asymptotic freedom as the effective coupling constant of the strong interaction decreases with increasing energy. In this case, quarks and gluons can be treated as free and their interactions can be calculated within perturbative theory. This is only allowed at short distance (equivalent to high energy), where the strong coupling constant converges asymptotically against zero. However, with increasing distance between two quarks (i.e. decreasing energy), the quarks become bounded in hadrons through a process called confinement.

2.2.2 Electroweak Theory

The full gauge group of the SM gauge theory is $SU(3) \otimes SU(2) \otimes U(1)$. Just as the non-Abelian group SU(3) gives rise to QCD, the non-Abelian group SU(2) and Abelian group U(1) give rise to the electroweak (EW) theory: the gauge theory behind the electroweak force. The electromagnetic and weak interactions can be unified under the $SU(2) \otimes U(1)$ symmetry group, and this is described by EW theory. The SU(2) group involves three gauge fields with a corresponding gauge bosons of W_μ^i with $i = 1, 2, 3$. The U(1) group involves a single gauge field and a corresponding gauge boson of B_μ . The Lagrangian of EW theory is

$$\mathcal{L}_{EW} = \sum_{j=1}^3 i\bar{\psi}_j(x)\gamma^\mu D_\mu \psi_j(x) - \frac{1}{4}B_{\mu\nu}B^{\mu\nu} - \frac{1}{4}W_{\mu\nu}^j W_j^{\mu\nu} \quad (7)$$

with $\sum_{j=1}^3 i\bar{\psi}_j(x)\gamma^\mu D_\mu \psi_j(x)$ corresponding to the fermion contribution and the remainder of the equation corresponding to the contribution from the gauge field. In this equation, the field strength tensors arise from the corresponding gauge bosons and have the following form

$$\begin{aligned} W_{\mu\nu}^i &= \partial_\mu W_\nu^i - \partial_\nu W_\mu^i + g\epsilon_{ijk}W_\mu^j W_\nu^k \\ B_{\mu\nu} &= \partial_\mu B_\nu - \partial_\nu B_\mu \end{aligned} \quad (8)$$

D_μ describes the covariant derivative

$$D_\mu = \partial_\mu - ig\frac{\sigma_j}{2}W_\mu^j(x) - ig'\frac{Y}{2}B_\mu(x) \quad (9)$$

with the coupling constants g and g' corresponding to SU(2) and U(1) respectively, and σ_j the j^{th} member of the Pauli matrices:

$$\sigma_1 = \begin{pmatrix} 0 & 1 \\ 1 & 0 \end{pmatrix}, \quad \sigma_2 = \begin{pmatrix} 0 & -i \\ i & 0 \end{pmatrix}, \quad \sigma_3 = \begin{pmatrix} 1 & 0 \\ 0 & -1 \end{pmatrix} \quad (10)$$

The fermionic half of the equation contains a term corresponding to the kinetic energy of the fermions along with the a covariant derivative term which describes the interaction of fermions with the gauge field. No explicit mass term for the fermions is allowed in this Lagrangian as such a term would result in a mixture of left-handed multiplets and right-handed singlets. As the weak interaction can only couple to left-handed fermions, this would require a violation of local gauge invariance which is forbidden.

Similarly to the fermionic half of the equation, the gauge field portion of the equation contains a term for kinetic energy and a term for the self interaction between the gauge fields. It is the non-Abelian nature of SU(2) that gives rise to this self interacting term. In order to avoid violation of the invariance of local gauge transformations, this portion of the Lagrangian also excludes any explicit mass term.

The four gauge bosons resultant of the SU(2)⊗U(1) symmetry group do not directly translate into the SM bosons of W^\pm , Z , and γ . W^\pm are linear combinations of W_μ^1 and W_μ^2

$$W_\mu^\pm = \frac{1}{\sqrt{2}}(W_\mu^1 \mp iW_\mu^2) \quad (11)$$

which represent the charged part of the interaction. Z and γ represent the neutral part of the interaction and evolve from the mixing of the W_μ^3 and B_μ neutral fields

$$\begin{pmatrix} A_\mu \\ Z_\mu \end{pmatrix} = \begin{pmatrix} \cos \theta_W & \sin \theta_W \\ -\sin \theta_W & \cos \theta_W \end{pmatrix} \begin{pmatrix} B_\mu \\ W_\mu^3 \end{pmatrix} \quad (12)$$

with the weak mixing angle θ_W .

2.2.3 Higgs Mechanism

The presence of the massive W^\pm and Z bosons within EW theory requires that these masses be accommodated in a gauge invariant and renormalisable manner: the Higgs mechanism [13][14].

In the Higgs mechanism, the spontaneous symmetry breaking of the quantum vacuum ground state generates the masses of the W^\pm and Z bosons while leaving the fundamental symmetry of EW theory unchanged. The Higgs mechanism introduces a complex scalar $SU(2)$ doublet ϕ with a hypercharge $Y = 1$

$$\phi(x) = \begin{pmatrix} \phi^{(+)}(x) \\ \phi^0(x) \end{pmatrix} = \sqrt{\frac{1}{2}} \begin{pmatrix} \phi_1(x) + i\phi_2(x) \\ \phi_3(x) + i\phi_4(x) \end{pmatrix} \quad (13)$$

Coupling ϕ to the gauge bosons allows a gauge invariant Lagrangian to be obtained:

$$L_{Higgs} = (D_\mu \phi)^\dagger D^\mu \phi - V(\phi) \quad (14)$$

using the covariant derivative D_μ defined in Eq 8. $V(\phi)$ describes the most general renormalisable potential invariant under an $SU(2)_L \otimes U(1)_Y$ gauge transformation

$$V(\phi) = \mu^2 \phi^\dagger \phi + \lambda (\phi^\dagger \phi)^2 \quad (15)$$

The potential is dependent upon the choice of μ and λ , as this selection constrains the bounds of the potential. In the instance where $\mu^2 < 0$ and $\lambda > 0$ the potential is bounded from below, and has a rotationally symmetric degenerate ground state

$$-\frac{\mu^2}{2\lambda} = \frac{v^2}{2} \quad (16)$$

where v describes the vacuum expectation value related to the Fermi constant G_F

$$v = \sqrt{\frac{1}{\sqrt{2}G_F}} \approx 246.22 \text{ GeV} \quad (17)$$

$\phi(x)$ is expanded using Eq. 12 via perturbation theory. The ground state can be fixed to $\phi_1 = \phi_2 = \phi_4 = 0$ and $\phi_3 = v$ at

$$\phi_0(x) = \frac{1}{\sqrt{2}} \begin{pmatrix} 0 \\ v \end{pmatrix} \quad (18)$$

as the choice of ground state is arbitrary when considering a rotation in phase space. The ground state is invariant with respect to a $U(1)_{em}$ symmetry (which is a subgroup of $SU(2) \otimes U(1)$). The Higgs $SU(2)$ doublet can be further expanded around the ground state $\phi_0(x)$, which results in

$$\phi(X) = \frac{1}{\sqrt{2}} \begin{pmatrix} 0 \\ v + H(X) \end{pmatrix} \quad (19)$$

Once the vacuum state of Eq. 14 is chosen, the underlying symmetry of $SU(2)_L \otimes U(1)_Y$ is spontaneously broken. The photon is left massless due to the remaining symmetry of $U(1)_{em}$. Three of the four degrees of freedom of EW theory are absorbed by the longitudinal polarization of the gauge bosons to form the massive W^\pm and Z^0 bosons. The remaining degree of freedom corresponds to the Higgs boson - a neutral scalar particle.

In summary, the above equations give the following Lagrangian for the Higgs field after spontaneous symmetry breaking has occurred:

$$\begin{aligned} L_{Higgs} = & \frac{1}{2} \partial_\mu H \partial^\mu H + const \\ & + \frac{1}{4} g^2 v^2 W_\mu^+ W^{-\mu} + \frac{1}{8} (g^2 + g'^2) v^2 Z_\mu Z^\mu - \lambda v^2 H^2 \\ & + \frac{1}{2} g^2 v H W_\mu^+ W^{-\mu} + \frac{1}{4} (g^2 + g'^2) v H Z_\mu Z^\mu \\ & + \frac{1}{4} g^2 H^2 W_\mu^+ W^{-\mu} + \frac{1}{8} (g^2 + g'^2) H^2 Z_\mu Z^\mu \\ & - \lambda v H^3 - \frac{1}{4} \lambda H^4 \end{aligned} \quad (20)$$

For each of the gauge bosons at tree level, a mass term can be determined directly from the Lagrangian

$$M_W = \frac{1}{2} v g = \frac{ev}{2 \sin \theta_W} \quad (21)$$

$$M_Z = \frac{1}{2} \sqrt{g^2 + g'^2} v = \frac{ev}{2 \sin \theta_W \cos \theta_W} = \frac{M_W}{\cos \theta_W} \quad (22)$$

$$M_\gamma = 0 \quad (23)$$

$$M_H = v \sqrt{2\lambda} \quad (24)$$

$$(25)$$

The vacuum expectation value is a direct factor of both the W and Z mass, hence it could be determined by measuring the masses of both bosons. The Higgs boson mass, however, cannot be calculated from the vacuum expectation value due to its dependence on λ which is a free parameter in the SM.

Fermion mass terms must be added via trilinear Yukawa couplings of the fermions to the Higgs fields, and this results in additional terms for the Lagrangian. These fermion masses are given by

$$m_f = \frac{1}{\sqrt{2}} g_f v \quad (26)$$

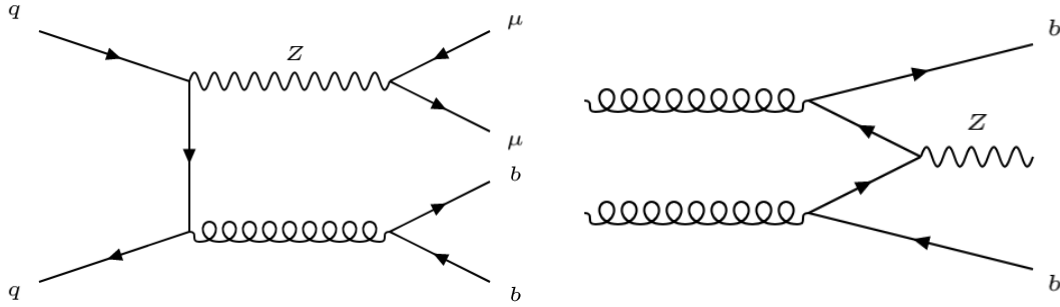
with the coupling constants g_f being free parameters of the SM.

2.3 Signal Processes

The signal process for $Z \rightarrow (\ell\ell) + b$ or $Z \rightarrow (\ell\ell) + bb$ contain events where the Z boson decays to two muons or two electrons ($Z \rightarrow (ee)$ or $Z \rightarrow (\mu\mu)$). This section describes the signal processes for $Z \rightarrow (\mu\mu)$ however the processes for $Z \rightarrow (ee)$ are similar, with the only difference being the decay products of the Z boson.

The most common production of a Z boson which decays to two muons is through the Drell-Yan process [15] - a quark-antiquark pair from two colliding protons annihilate and produce two muons through the weak force mediated by a Z boson. However, in order to arrive at the final state either of the signal processes for this analysis ($Z \rightarrow (\mu\mu) + b$ or $Z \rightarrow (\mu\mu) + bb$), an additional requirement must be met - the presence of one or two b-quarks.

The most common mechanism for this process to occur is for one of the annihilating quarks to radiate a gluon. The gluon then produces a pair of b-quarks (with one a standard b-quark, and the other an anti b-quark), meeting the requirements for the final state of the process. The Feynman diagram of this process can be seen in Figure 2.2a.



(a) $q\bar{q}$ annihilation in conjunction with the radiation of a gluon.

(b) The final state produced by interactions of a gluon pair.

Figure 2.2: A figure showing two possible mechanisms by which a $Z \rightarrow (\mu\mu) + bb$ final state can be achieved.

Another dominant process for this production is a pair of gluons producing two quark-antiquark pairs. Each of the two gluons produces a $b\bar{b}$ pair, and interaction

between the two pairs allows two of the quarks to annihilate and produce a Z boson (which later decays to two muons). The Feynman diagram for this process can be seen in Figure 2.2b.

Finally, another process to be considered is that of the Compton process by which the interaction of a gluon with a single quark radiates a Z boson. It is this process that allows for the insight into the structure of the proton. At any one time, the content of a proton can be described by its PDF.

The PDF of a given parton is a function of two variables: the fraction of the proton momentum carried by a parton (x), and the "scale" corresponding to the energy at which the parton is probed (Q^2). As the protons are collided inside the LHC beamline, the sea-quarks within the proton are able to interact with other partons such as valence quarks and gluons. For example in the case of $Z \rightarrow (\mu\mu) + b$, the gluons and quarks interact via a hard process to produce a final state with one b-quark and a Z boson, which is subsequently detected by ATLAS. The cross section for this hard process can be written in the following form:

$$\frac{d\sigma}{dQ^2} = \sum_{i,j \in \{q, \bar{q}, g\}} \int dx_1 \int dx_2 f_i(x_1, Q^2) f_j(x_2, Q^2) + f_i(x_2, Q^2) f_j(x_2, Q^2) \frac{d\hat{\sigma}_{ij}}{dQ^2} \quad (27)$$

With $\hat{\sigma}_{ij}$ as the cross section for (anti)-quarks and/or gluons, where i and j label the species of the colliding particle, and $f_i(x, Q^2)$ the probability to find a particle of type i carrying a fraction x of the proton momentum[16]. When the process is detected, the momentum of the incident quarks can be calculated and used to perform a measurement of the proton PDF. PDFs are useful for calculating the cross sections of physical processes, and a measurement of $Z \rightarrow (\mu\mu) + b$ allows for a measurement of the proton PDF as well. The Feynman diagram for this process can be seen in Figure 2.3.

2.4 Background Processes

As with the signal processes, the background process for $Z \rightarrow (\ell\ell) + b$ and $Z \rightarrow (\ell\ell) + b\bar{b}$ are almost identical for both $Z \rightarrow (ee)$ and $Z \rightarrow (\mu\mu)$ with the only difference being the decay products of the Z boson. This section describes the processes for $Z \rightarrow (\mu\mu)$.

The difficulty of $Z \rightarrow (\mu\mu) + b\bar{b}$ analysis is in no small part due to the number of background processes that make a direct measurement difficult. In order to obtain a clear and accurate measurement of the signal process, there must be an equally clear understanding of the background processes such that any effect they have on a measurement of the signal process can be modelled and removed.

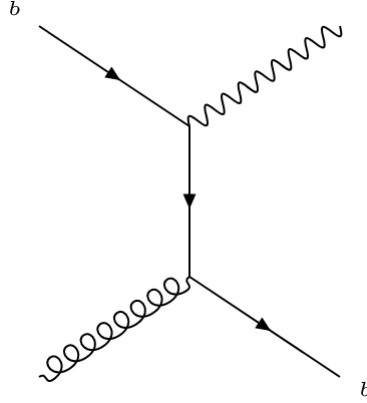
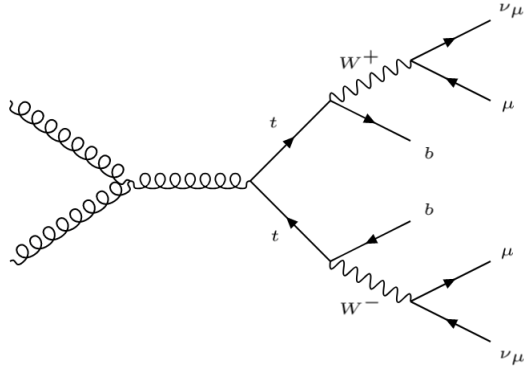
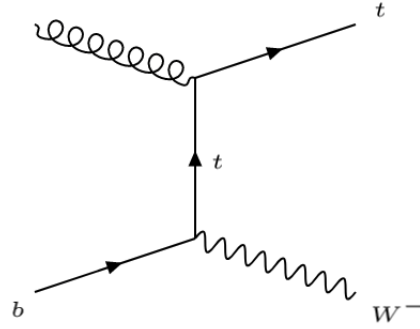


Figure 2.3: A figure showing the Feynman diagram for the Compton Process.

The first and most common of these background processes is the top quark pair background. A pair of top quarks (specifically $t\bar{t}$) are produced through one of many potential mechanisms, such as via a gluon interaction. Each top quark then undergoes a weak interaction to become a b quark, and produces a muon via a W boson and weak decay (as the overall charge of the process must be conserved). This results in the same final state as the $Z \rightarrow (\mu\mu) + b\bar{b}$ signal process plus two additional neutrinos from the weak interaction of each top quark to a bottom quark. The Feynman diagram for this process can be seen in Figure 2.4a.



(a) The Top Quark Pair Production background process.



(b) The Single Top background process.

Figure 2.4: A figure showing the Feynman diagrams of Top Quark Pair Production and Single Top background production.

Another background process dependent on a charged current interaction is the single top background process. An incoming b-quark interacts with a gluon and experiences a weak interaction. A W boson is produced alongside a top quark, corresponding to the weak interaction of the b-quark. This results in the emission of only a single top quark,

along with a W boson. This process can be seen in Figure 2.4b. The final state is achieved by the weak interaction of first the top quark, which produces the necessary b-quark and an additional W boson, followed by the leptonic decay of two W bosons which produce a muon and a neutrino each.

In addition to these background processes are the diboson background processes. In these interactions, annihilating quarks produce a combination of two bosons which produce the required final state particles. The first of these processes is referred to as ZqqZll, in which both of the bosons produced are Z bosons. One Z boson decays to two leptons, and the second decays to two quarks. The most common source of this background in $Z \rightarrow (\mu\mu) + b\bar{b}$ production is the case where one Z boson decays to two muons, and the other to two b-quarks. This process can be seen in Figure 2.5a.

The second of these diboson processes is referred to as WqqZll. This process is similar to the ZqqZll process, however in this instance only one of the produced bosons is a Z boson and the other is a W boson (as opposed to both being Z bosons). In this case, the W boson decays to two quarks, and the Z boson to two leptons. The most common form that this background process takes in the $Z \rightarrow (\mu\mu) + b\bar{b}$ analysis is the case where the W boson decays to a bottom quark and a charm quark, and the Z boson decays to produce two muons. This immediately fulfils the final state of the $Z \rightarrow (\mu\mu) + b\bar{b}$ processes, and can easily imitate the $Z \rightarrow (\mu\mu) + b\bar{b}$ process if the charm quark is mistagged as a b-quark. These background processes (WqqZll and ZqqZll) are a small yet common background that is consistently present across the full energy range of the analysis. The Feynman diagram for these processes can be seen in Figure 2.5.

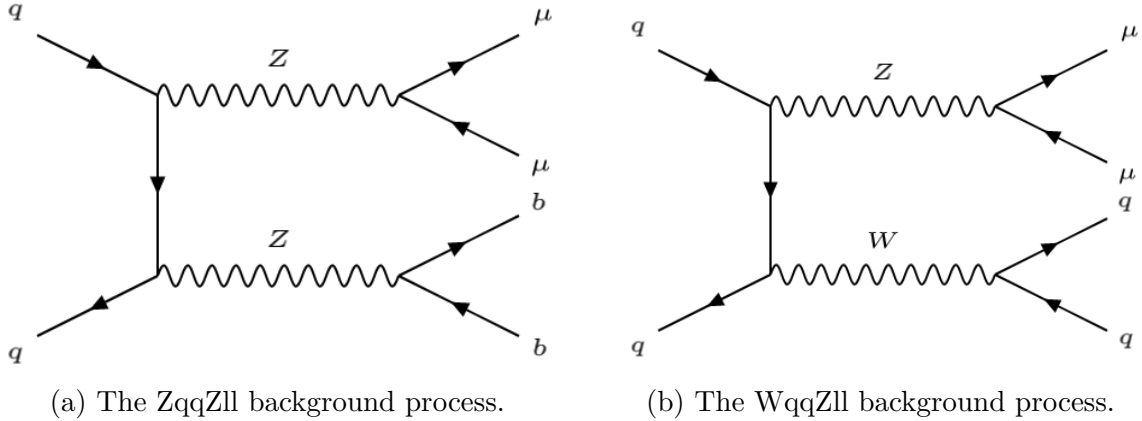


Figure 2.5: A figure showing the Feynman diagrams for the WqqZll and ZqqZll background processes.

In addition to the WqqZll and ZqqZll backgrounds mentioned above, there is an additional background process named ZZ4l which corresponds to an event where the two produced Z bosons decay into four leptons. The Feynman diagram for this process can be seen in Figure 2.6. This background process occurs when one of the Z bosons

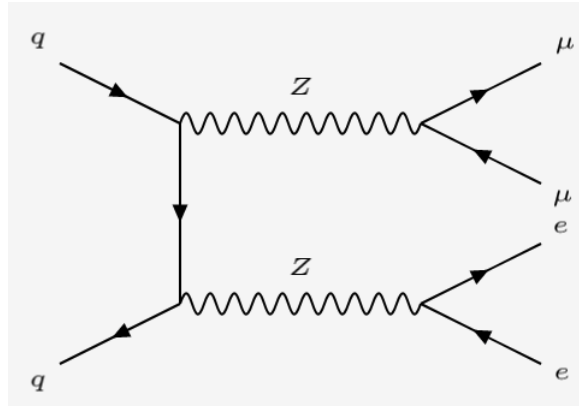


Figure 2.6: The ZZ4l background process.

produces two muons, and the other two electrons. Electrons produce jets along with electromagnetic showers within the electromagnetic calorimeters in ATLAS (see section 3.2.3), and a background process is found where this reconstructed jet is mistagged as a b-jet.

3 LHC and ATLAS

The source of all experimental data within this thesis is the ATLAS experiment at the Large Hadron Collider (LHC). The following chapters will provide an introduction to both the LHC and the ATLAS experiment with a primary focus on the subsystems of the ATLAS detector most relevant to this analysis. The data used in this thesis was collected during the second run of data collection by the LHC (appropriately named Run 2), which concluded in December of 2018. The third run of data collection will begin in 2021.

3.1 LHC

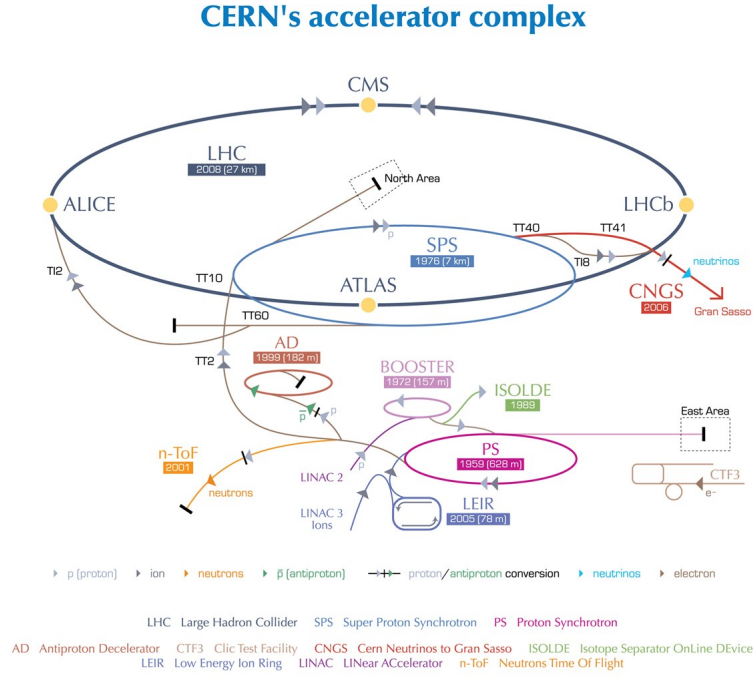
100 meters beneath the site of the Conseil Européen pour la Recherche Nucléaire (CERN) at the French-Swiss border near Geneva, Switzerland lies the LHC. At approximately 27 kilometres in circumference, the LHC accelerates beams of protons to the highest energies in the world reaching speeds greater than 99.9% the speed of light [17–19].

3.1.1 Acceleration at the LHC

Beginning with its initial flagship accelerator, CERN has constantly upgraded its accelerators and included the work of previous experiments in each new effort to collect even greater amounts of particle collision data. The full acceleration of the particle beams within the LHC is not reliant on a single static machine but a combined effort from multiple component accelerators, each of which further accelerates beams of particles to higher and higher energies prior to collision. Each particle accelerated by the LHC experiences not just a chain of particle accelerators, but a timeline of CERN’s remarkable history.

This chain of accelerators begins with an ordinary container of hydrogen: atoms of hydrogen are extracted from the canister and subjected to an ionising electric field, stripping the hydrogen atoms of their electrons and leaving only the protons remaining. This ionised hydrogen gas is then immediately fed into the Linear Accelerator 2 (LINAC2), which accelerates the protons up to an energy of 50 MeV. LINAC2 has been in operation since 1978 after replacing the original Linear Accelerator 1 (LINAC1), and will itself be replaced by the Linear Accelerator 4 (LINAC4) in Run 3 to further upgrade the LHC [20].

Following their linear acceleration through LINAC2, the protons then enter the first of the four circular accelerators within the LHC acceleration chain: the Proton Synchrotron Booster (PSB). The PSB accelerates the protons to an energy of 1.4 GeV, before injecting them into the Proton Synchrotron (PS) which increases the energy of



European Organization for Nuclear Research | Organisation européenne pour la recherche nucléaire

© CERN 2008

Figure 3.1: A figure showing the arrangement and relative sizes of the accelerators within the LHC acceleration chain [23].

the protons to 25 GeV. The PS first accelerated protons on 24 November 1959, serving as CERN's first synchrotron. While the PS has been heavily modified from its original state, it still serves as a key piece of LHC operations over 60 years later.

From the PS, the protons are then injected into the even more powerful Super Proton Synchrotron (SPS): far larger than the 688 m circumference of the PS, the SPS has a circumference of 7 km and almost 5 times as many electromagnets, capable of accelerating the protons to an energy of 450 GeV. The SPS originally operated as the principle collider of CERN's particle physics program when it came online in 1976 and was crucial in several key experiments in CERN's history, such as the Nobel-prize-winning discovery of the W and Z bosons in 1983 when the SPS ran as a proton-antiproton collider [21, 22].

The final step in the accelerator chain is the LHC itself, however the method of accelerating within the LHC differs slightly from the techniques of the previous circular accelerators. The protons from the SPS are injected to the LHC at two points instead of one in order to create two separate proton beams which circulate in opposite directions. These two distinct beams are each accelerated up to an energy of 6.5 TeV, allowing for a centre-of-mass energy of $\sqrt{s} = 13$ TeV during Run 2. The full chain of LHC accelerators can be seen in Figure 3.1.

Achieving the acceleration required to achieve these energies is no easy task. The tunnels in which the LHC resides were originally constructed for the Large Electron-Positron (LEP) collider [24–27], a particle-antiparticle collider capable of accelerating two beams in opposite directions with the same magnetic field (due to the opposite charge between a charged particle and its respective antiparticle). The same method cannot be applied in the case of proton-proton collisions as the charge of each beam will be the same. Instead, the LHC uses its single magnet system to produce a pair of coupled magnetic fields which have an opposing polarity.

The LHC does not, however, accelerate the particle beams at every point along its circumference. The LHC is composed of 8 octants, in which the LHC ring is actually a straight line. The curvature of the particle beams occurs at the boundaries of each octant, where 1232 powerful dipole magnets (each 15 metres long and with a weight of 35 tonnes) create a magnetic field of 8.3 T which bends the beams towards the centre of the LHC ring. These dipoles work in conjunction with 392 quadrupoles: magnets with alternating poles in a symmetrical layout that help focus the beam [28]. In order to remain superconducting, these magnets are cooled with super-fluid Helium which allows the magnets to operate at 1.4 K.

The straight sections of the LHC within each of the octants are referred to as "Points", and are numbered according to their position around the LHC ring. Each of these points can be seen in Figure 3.2. Point 1, Point 2, Point 5, and Point 8 contain each of the interaction points (IPs) where the particle beams cross and interactions occur. Four large particle detectors of varying design are constructed at each of these IPs in order to observe the collisions that occur where the particle beams collide: two large general-purpose experiments ATLAS [29] and CMS [30] at Point 1 and Point 5, the ALICE [31] experiment at Point 2 primarily examining heavy-ion collisions, and the LHCb [32] experiment at Point 8 primarily exploring flavour physics and CP-violation through bottom and charm quarks.

Point 3 and Point 7 contain the beam cleaning and collimation systems, essential systems that protect the components of the LHC. As proton beams travel around the LHC ring, they do not exist as a single line; some protons are unavoidably lost from the focussed central beam core and diffuse into a "beam halo", the fraction of the beam that will physically collide with the components of the LHC. These collisions from the beam halo can damage these components: for example, collisions with the LHC's superconducting magnets could cause a rise in temperature forcing the magnets out of a superconducting state (this is known as a magnet "quench") [34]. The collimator systems restrict the potential aperture of the beam, deliberately causing collisions with the beam halo to occur safely in the collimators (instead of in the LHC's more delicate subsystems) [35].

The beam dump is located at Point 6, and is another important subsystem for the efficiency and safety of the LHC. When the particle beam within the LHC has served its

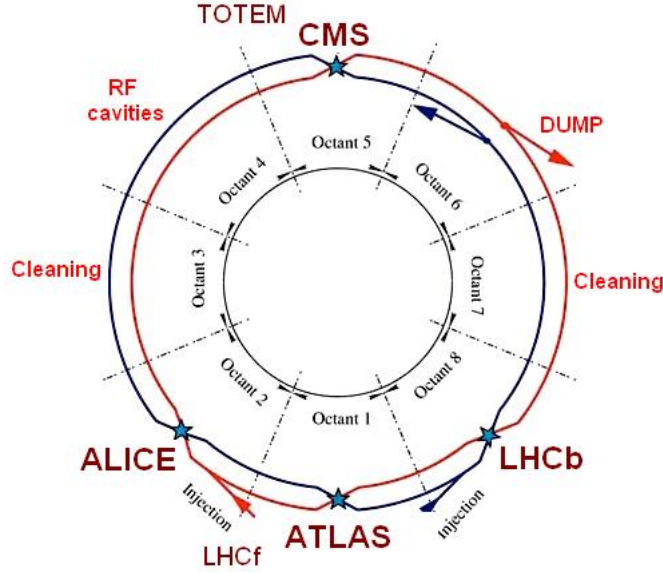


Figure 3.2: A figure showing the arrangement of the LHC octants or "Points" [33].

purpose, the beam (or the remnants of it) needs to be safely removed from the LHC ring. The beam may also be dumped in the event of instability observed by the LHC or one of the detectors observing each of the IPs, or in the event of issues with one of the detectors. In the event that the beam needs to be dumped for any of these reasons, the LHC employs the use of kicker magnets that rapidly and safely diver the beam out of the LHC ring and into dump blocks: cylinders of graphite encased in concrete that can absorb the full energy of the beam without melting [18].

The actual acceleration of the particle beam within the LHC occurs at the superconducting radio-frequency (RF) cavities located at Point 4. The LHC employs 8 RF cavities per beam, which use an alternating electric field to accelerate the beam through the cavity. By increasing the frequency of these oscillations, the particle beam can gradually increase to its maximum energy. Much like the dipole and quadrupole magnets used within the LHC, the RF cavities also operate at an extremely low temperature (4.5 K). The accelerating field provided by the RF cavities is 5 MV/m at 400MHz [36]. Accelerating particles using the alternating electric field of the RF cavities causes the particle beam not to be a single continuous beam, but to instead be divided into *bunches*.

3.1.2 Beam Structure

When the particle beam passes through the RF cavities, some of the particles synchronize exactly with the RF frequency (these particles are aptly named "synchronous particles"). Particles that do not exactly synchronize with this frequency

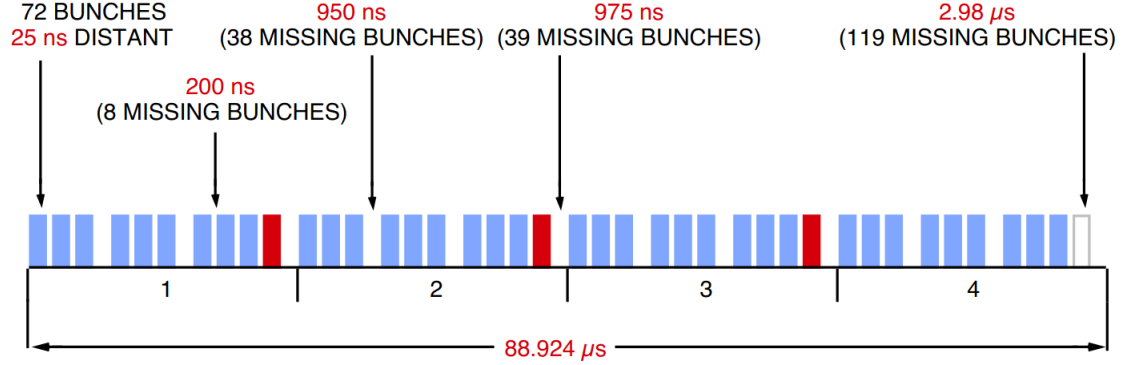


Figure 3.3: A figure showing the arrangement of the PS trains within the final SPS batch injected into the LHC [38].

instead become clustered around the synchronous particle, and this travelling group of synchronized particles is referred to as a bunch. In order to allow for the necessary time for its subsystems to function correctly, the LHC beam is not a continuous stream of bunches but a combination of bunches and "missing" bunches (deliberate absences of bunches used primarily for timing).

The nominal LHC beam consists of 2808 bunches, each consisting of 1.15×10^{11} protons [17, 19]. The PS supplies particles to the SPS and LHC in the form of 72-bunch PS trains, with each bunch arriving 25ns apart [37]. When these bunches are accelerated by the SPS and enter into the LHC, they are arranged into the form of 3, 3, and then 4 PS trains. The very last PS train in the very last SPS batch is deliberately suppressed to allow time for the LHC extraction kicker magnets (required in the event of a beam dump) to rise. This bunch structure can be observed in Figure 3.3.

3.1.3 Luminosity

In order to evaluate the performance of an accelerator, it is important to consider a metric that adequately describes the collisions taking place. In the case of accelerator physics *luminosity*, a measure of how effectively an accelerator is able to deliver particle collisions, is used. For a process with a known cross section of σ_i , the event rate is given by:

$$\frac{dN}{dt} = \mathcal{L}_i \sigma_i \quad (28)$$

where \mathcal{L}_i is the instantaneous luminosity. The instantaneous luminosity (i.e. the luminosity of two colliding particle beams at any single instant) is useful for the measuring performance during stable collisions, although the quantity of integrated luminosity is typically more useful for measuring performance across a complete period

of data collection. The integrated luminosity of an accelerator is defined as the integral of the accelerator's instantaneous luminosity with respect to time, i.e. the instantaneous luminosity at every instant or:

$$\mathcal{L}_{int} = \int \mathcal{L}_i dt \quad (29)$$

Instantaneous luminosity is defined as:

$$\mathcal{L}_i = \frac{N_1 N_2 k f \gamma}{4\pi \epsilon_n \beta^*} F \quad (30)$$

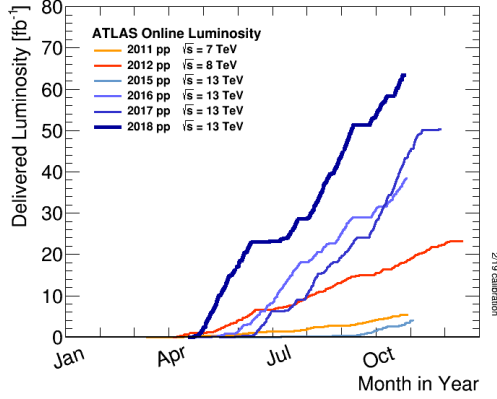
where:

- N_1 and N_2 represent the number of protons within each colliding particle bunch
- k is the number of bunches per beam
- f is the frequency of the colliding beams (the nominal value of which is 11.245 kHz at the LHC)
- γ is the relativistic Lorentz factor of the accelerated particles
- ϵ_n is the beam emittance (i.e. average spread of particles within the beam)
- β^* is the beta function of the beam (i.e. the amount that the beam is "squeezed")
- F is a geometric correction due to the crossing angle of the beams

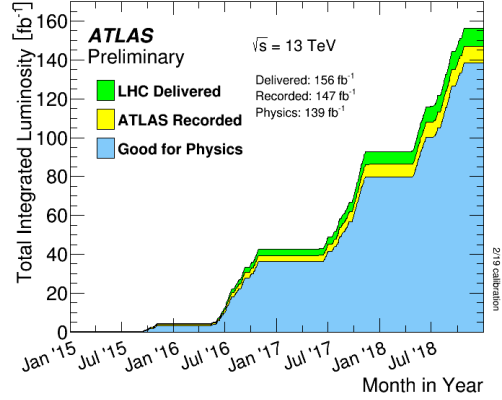
Instantaneous luminosity is expressed in units of $\text{cm}^{-2}\text{s}^{-1}$. The peak instantaneous luminosity of the LHC was designed to reach a value of $1 \times 10^{34} \text{cm}^{-2}\text{s}^{-1}$, however this value has been exceeded and peak instantaneous luminosities of up to $2.1 \times 10^{34} \text{cm}^{-2}\text{s}^{-1}$ have been achieved.

Integrated luminosity has units of cm^{-2} but is more commonly expressed in units of inverse femtobarn fb^{-1} where one barn (1 b) is equivalent to $1 \times 10^{-28} \text{m}^{-2}$. During Run 2 the ATLAS detector recorded a total of 139.9fb^{-1} of luminosity usable for physics analyses corresponding to 3.2fb^{-1} in 2015, 32.9fb^{-1} in 2016, 43.7fb^{-1} in 2017, and 60.1fb^{-1} in 2018 [39].

This analysis uses the full 139.9fb^{-1} luminosity of good data recorded by ATLAS during Run 2. The total amount of data recorded by ATLAS during Run 2 is greater than this figure at 146.9fb^{-1} , however not all of this data is suitable for physics analyses (such as in the event that not all detector subsystems are online). A visualisation of the luminosity delivered to and recorded by the ATLAS detector from the LHC can be seen in Figure 3.4.



(a) Delivered luminosity vs. time



(b) Total integrated luminosity vs. time

Figure 3.4: (a) Cumulative luminosity versus month delivered to ATLAS during stable beams and for high energy p-p collisions. (b) Cumulative luminosity versus time delivered to ATLAS (green), recorded by ATLAS (yellow), and certified to be good quality data (blue) during stable beams for pp collisions at 13 TeV centre-of-mass energy in 2015-2018 [39].

3.1.4 Pileup

In the collision of two nominally filled bunches there are a total of 2.3×10^{11} protons available to collide, allowing a high number of hard pp interactions. Ideally the experiments at CERN would only record these hard interactions however this is not always the case, as additional interactions between bunches can occur. These additional interactions are referred to as pileup and can cause a multitude of issues in the reconstruction of hard events such as track mis-reconstructions, degradation of object resolution, and ambiguity in primary vertex location.

Pileup can be categorised into two types:

- **In-time** pileup refers to other interactions within *the same* bunch as the hard interaction.
- **Out-of-time** pileup refers to interactions within *other* bunches relative to the hard interaction.

Pileup is quantified by use of $\langle \mu \rangle$, the average number of interactions per bunch crossing. This value corresponds to the mean of the poisson distribution of the number of interactions per crossing calculated for each bunch, calculated from the instantaneous per bunch luminosity which is given by the equation:

$$\mu = \frac{\mathcal{L}_{bunch} \times \sigma_{inel}}{f} \quad (31)$$

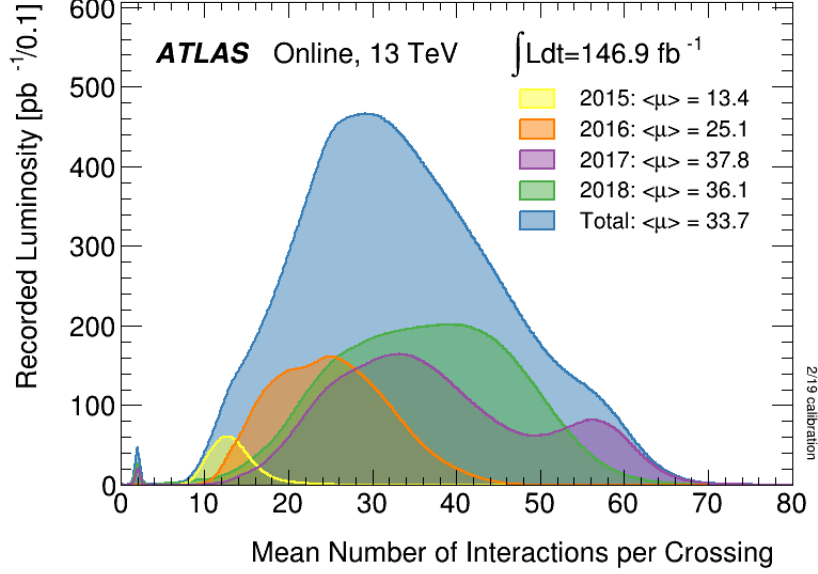


Figure 3.5: A figure showing the average interactions per bunch crossing for all ATLAS data recorded during Run 2 [39].

where \mathcal{L}_{bunch} is the per bunch instantaneous luminosity, σ_{inel} is the inelastic cross section (taken to be 80 mb for $\sqrt{s} = 13\text{TeV}$ collisions), and f is the LHC revolution frequency of 11.245 kHz. The full pileup profile of Run 2 can be seen in Figure 3.5. The pileup profile uses the full 146.9fb^{-1} of online data recorded by ATLAS during Run 2 as opposed to the 139.9fb^{-1} of physics data, which can be seen in Figure 3.4b.

3.2 ATLAS

The ATLAS (A Toroidal LHC ApparatuS) experiment [29], located at Point 1 of the LHC ring, is the largest general-purpose experiment at CERN. The design of ATLAS is carefully engineered in order to maximise its capabilities as a general-purpose particle detector [40–42]. ATLAS is cylindrical in shape, with a length of 46 metres and a diameter of 25 metres. The immense scale of ATLAS can be difficult to picture without adequate reference: the diameter of ATLAS is 1 metre greater than the height of Buckingham palace, and its length is the same as the Statue of Liberty’s height¹. It would take a tower of 9 giraffes carefully lying head to hoof in the ATLAS cavern while wearing the appropriate personal protective equipment (PPE) to occupy the same length as the ATLAS detector².

The ATLAS detector is constructed around the LHC beamline at Point 1 with its

¹The statue of liberty itself, excluding the 47 m pedestal that the statue stands upon.

²This would likely irritate the giraffes.

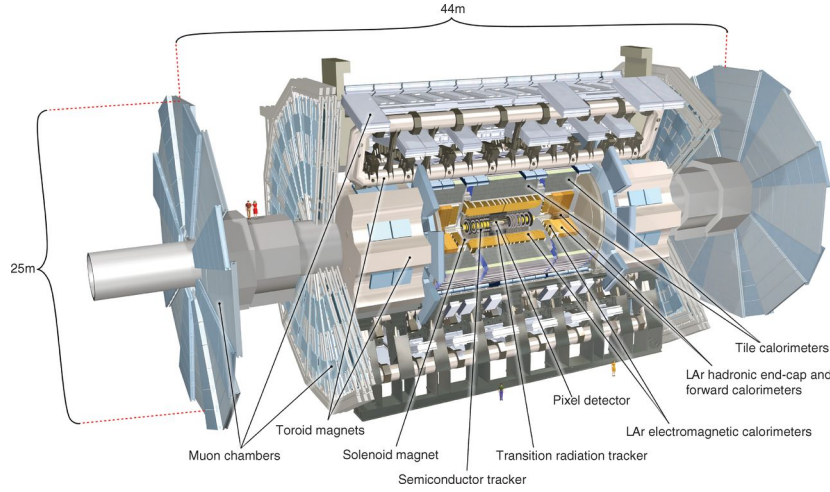


Figure 3.6: A figure showing the subsystems of the ATLAS detector [42].

cylindrical geometry divided into two categories: the *barrel* and the *end-cap*, which can be visualised as the sides and top/bottom of a standard cylinder respectively. The cylindrical design of the ATLAS detector allows almost full coverage of 4π and forward-backward symmetry across the IP, hence the IP is located at the perfect centre of the barrel region in the heart of the detector. Particles originating from collisions at the IP travel outward and through different sub-systems, each sensitive to particular properties of various particles, in order to identify and reconstruct physics objects in each event.

The **Inner Detector (ID)**, the sub-system closest to the IP, tracks the path of all charged particles that pass through it. For particles travelling outward from the IP the next sub-system encountered are the **ATLAS Calorimeters** which aim to stop both hadronic and electromagnetic particles in order to measure their energy. Finally, the remaining particles from events at the IP pass through the outermost sub-system: the Muon Spectrometer (MS), which aims to identify and track the path of muons. All of these systems are subjected to a magnetic field generated by the ATLAS magnet systems: a solenoid magnet creates the field beyond the ID, and the eponymous toroidal magnet creates the magnetic field beyond the calorimeters. A cross section of ATLAS and these detector sub-systems can be seen in Figure 3.15.

3.2.1 The ATLAS Coordinate System

In order to be able to accurately describe events relative to the detector and interaction point, ATLAS uses a well defined right-handed coordinate system. Taking the nominal IP as the origin, the x -axis points towards the centre of the LHC ring, the y -axis points vertically upwards, and the z -axis points along the direction of the beam pipe. A subtle yet crucial result of this coordinate system is the definition of the x - y plane, which is

tangential to the beam pipe (referred to as the *transverse* plan). The nature of the fundamental colliding partons prevent the initial momentum in the z direction from being known, however it is known that the partons have zero initial momentum in the transverse plane and therefore directional vector quantities such as momenta can be projected into the transverse plane.

In addition, cylindrical coordinates are used to describe the geometry of the detector. The azimuthal angle, ϕ , describes the angle around the beam direction in the transverse plane where $\phi = 0$ points in the same direction as the x -axis (i.e. towards the centre of the LHC ring). The polar angle, θ , describes the angle from the beam direction in the y - z plane where $\theta = 0$ points in the same direction as the z axis (i.e. along the beam pipe). The final coordinate of the ATLAS coordinate system is the rapidity (y) or pseudorapidity (η). The rapidity of a particle is defined as:

$$y = \frac{1}{2} \ln \left(\frac{E + p_z}{E - p_z} \right) \quad (32)$$

where E is the particle's energy and p_z is the momentum of the particle in the z axis. The pseudorapidity of a particle is defined in terms of the polar angle, θ , as:

$$\eta = -\ln \tan \left(\frac{\theta}{2} \right) \quad (33)$$

Pseudorapidity is typically used in place of θ as it is Lorentz invariant under a boost in the z -axis whereas θ is not. The rapidity and pseudorapidity are equivalent for massless particles and this holds true for particles with extremely small mass (several orders of magnitude lower than their average energy) such as electrons. The angular distance between two objects is described using the variable ΔR , which is also Lorentz invariant under a boost in the z -axis. ΔR is defined by the relation:

$$\Delta R = \sqrt{(\Delta\eta)^2 + (\Delta\phi)^2} \quad (34)$$

3.2.2 The Magnet System

The ATLAS magnet system consists of four magnets: a single solenoid magnet [43], and three toroidal magnets [44, 45] (which contribute an important part of the ATLAS name). The central solenoid provides the magnetic field for the inner detector, and the toroidal magnets provide the magnetic field for the muon system. The arrangement of the magnet systems within ATLAS can be seen in Figure .

The solenoid magnet is named the Central Solenoid Magnet. It is aligned with the z -axis (i.e. the beam pipe) and exerts a 2T axial magnetic field which bends the path of charged particles within the inner detector. The magnet weighs 5 tonnes but is only 5

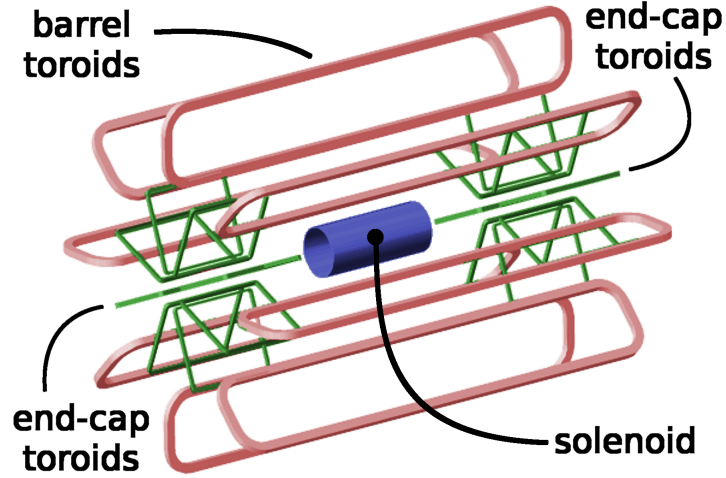


Figure 3.7: The relative location of the solenoid, barrel toroids, and end-cap toroids [46].

cm thick (which corresponds to 0.66 radiation lengths) in order to minimize the probability of particle interactions with the magnet itself. The solenoid is cooled to a temperature of 4.5 K in order to maintain its superconducting state, and is capable of storing a total of 38 MJ of energy.

In the case of the toroidal magnets, there is one toroidal magnet located in the barrel region and one toroidal magnet in each end-cap region. The magnetic fields produced by the toroids are orthogonal to each other, creating an overall magnetic field of 0.5 T in the barrel region and 1 T in each end-cap. Together, these magnetic fields bend the path of muons in the outermost region of the detector. The position of each toroid's coils can be seen in Figure 3.7. Each magnet contains eight coils, however the coils for the barrel region are by far the largest with a length of 25.3 metres each whereas the length of the end-cap coils are only 5 metres. Each end-cap toroid weighs 240 tonnes and stores 0.25 GJ of energy, while the much larger barrel toroid weights a total of 830 tonnes and stores a total of 1.08 GJ of energy.

The shape of the magnetic field created within ATLAS by both the solenoid and toroidal magnet can be seen in Figure 3.16.

3.2.3 The Inner Detector

The Inner Detector [48, 49] is the most central component of ATLAS providing precise measurements of both particle charge and momentum, in addition to tracking charged particles to a pseudorapidity range of $|\eta| < 2.5$. Using both an impact parameter, d_0 , and a longitudinal impact parameter, z_0 , the ID is able to characterise the primary vertex of each interaction. The parameter d_0 is defined as the distance between the vertex's point of closest approach and the z -axis, and the parameter z_0 is defined as the

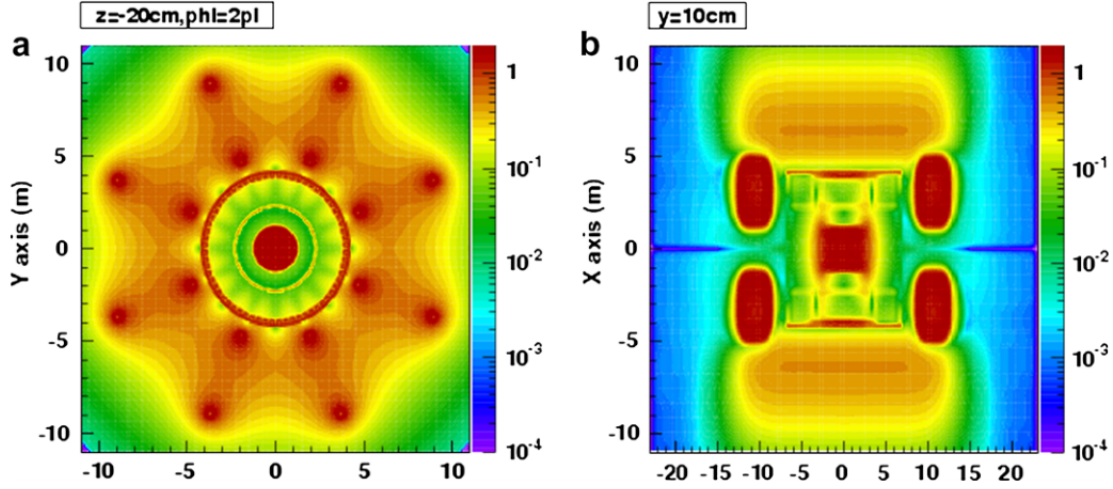


Figure 3.8: The shape of the magnetic field within the ATLAS detector. The left plot shows the magnetic field as if looking down the beamline. The right plot shows the magnetic field when viewed from above [47].

z -coordinate of the primary vertex's point of closest approach. A high precision measurement of the primary vertex is crucial to this analysis as the delayed secondary vertex of b-tagged events is an extremely important in their identification, and an excellent resolution for d_0 and z_0 allows for easier identification of b-hadrons and other particles with longer lifetime. The layout of these components within the ID barrel region can be seen in Figure 3.17.

The ID consists of four subsystems which work in conjunction to track charged particles and perform high resolution measurements of their charge and momentum. These subsystems are the [Insertable B-Layer \(IBL\)](#), the [Pixel Detector](#), the [Semiconductor Tracker \(SCT\)](#), and the [Transition Radiation Tracker \(TRT\)](#). A cross section of these systems within the ID can be seen in Figure 3.10.

The IBL, pixel detector, and SCT all operate through the use of pixel modules containing tens of thousands of silicon pixel sensors. As charged particles pass through the pixel sensors, they ionise with the silicon semiconductors, freeing electrons from atoms within the silicon and creating ion-electron pairs. By interpreting the resultant signal created at the points within these pixel modules that these ion-electron pairs are created, the path of the charged particles that pass through the ID can be measured.

3.2.3.1 The Insertable B-Layer (IBL)

The most central component of the ID is the IBL [51] (positioned a mere $R = 33.25$ mm away from the beam pipe), which was added to ATLAS during the shutdown between

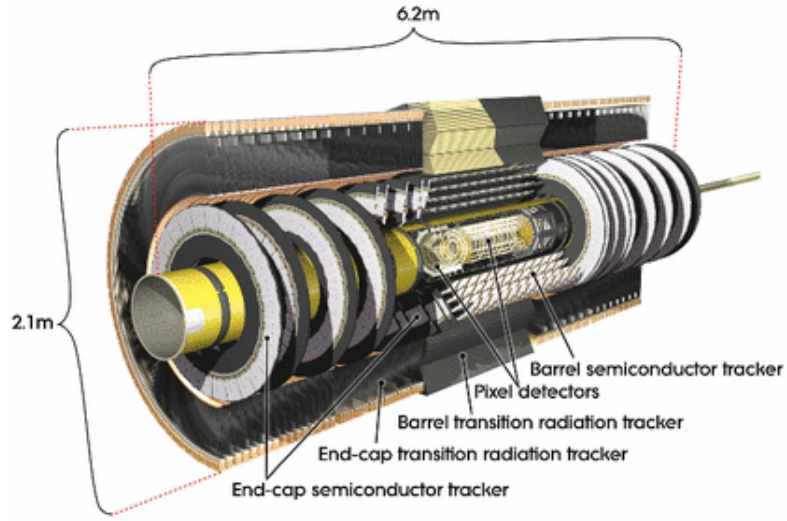


Figure 3.9: A figure showing a cut-away view of the ATLAS inner detector and its components [50].

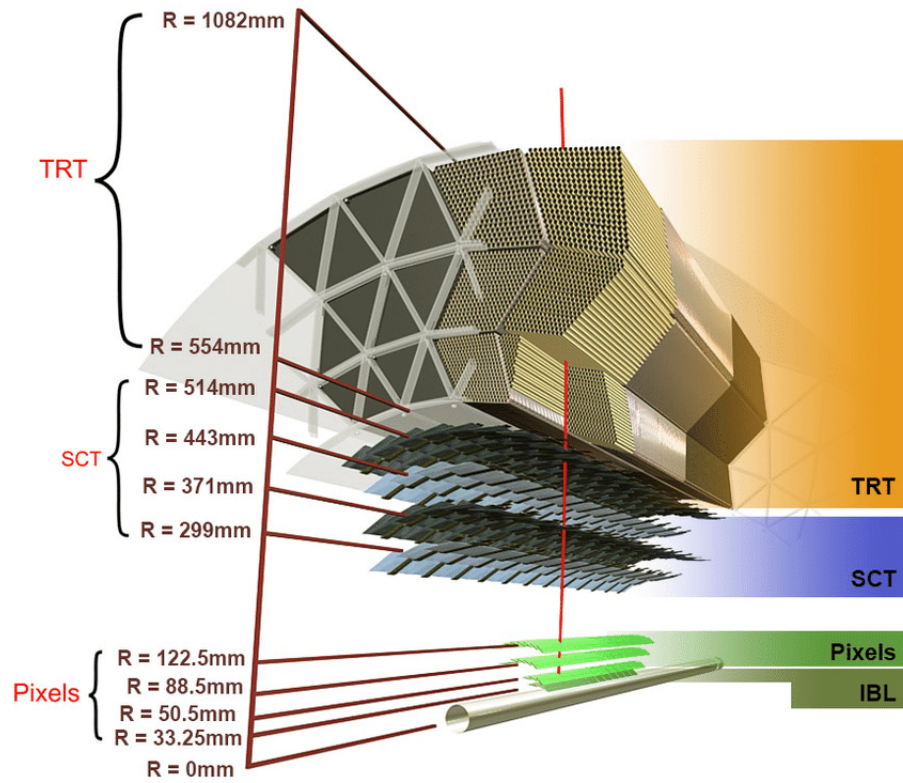


Figure 3.10: A figure showing a cross section of the ATLAS inner detector barrel region and its components [50].

Run 1 and Run 2. The IBL increases the resolution of d_0 and vertex measurements when compared with the pixel detector alone, which is an important addition due to the high pileup of Run 2 (which can easily obfuscate the primary vertex as discussed in Section 3.1.4). Each individual pixel is extremely small and has dimensions of $50\mu\text{m} \times 250\mu\text{m}$, which allows for a tracking resolution of $8\mu\text{m}$ and $40\mu\text{m}$ in the x - y plane and z direction respectively.

3.2.3.2 The Pixel Detector

The pixel detector consists of three layers of concentric cylinders coaxial to the beam pipe, and three layers of end-cap disks perpendicular to the beam pipe. The barrel layers are positioned at $R = 50.5, 88.5, \text{ and } 122.5$ mm, with the end-cap disks positioned at $z = 495, 580, \text{ and } 650$ mm. These components consist of a total of 1744 pixel modules [52] with a thickness of $250\mu\text{m}$, each containing 47,232 pixels with dimensions of $50\mu\text{m} \times 400\mu\text{m}$. Each pixel module contains 16 front-end chips with 2880 readout channels equating to a total of 46,080 readout channels per module, however all 47,232 pixels are readout of each module (pixels in the inter-chip regions are ganged together to be readout). Overall, the pixel detector has over 80 million readout channels and provides a spatial resolution of $10\mu\text{m}$ in the x - y plane and a spatial resolution of $115\mu\text{m}$ in the z -axis.

3.2.3.3 The Semiconductor Tracker (SCT)

The Semiconductor Tracker (SCT) [53] sits outside the pixel detector and is similar in operation, consisting of 4 barrel layers and 9 end-cap disks. The barrel layers are positioned at $R = 299, 371, 443, \text{ and } 514$ mm, and the end-cap disks range from $z = 854 - 2720$ mm. The 15,912 strip modules have a thickness of $285\mu\text{m}$ and consist not of pixels as per the pixel detector but 768 silicon strips each 12 cm long, necessitating over 6.4 million readout channels. In total the SCT contains 61 m^2 of silicon strip sensors, and provides a hit resolution of $17\mu\text{m}$ in the x - y plane and a hit resolution of $580\mu\text{m}$ in the z -axis.

3.2.3.4 The Transition Radiation Tracker (TRT)

The Transition Radiation Tracker (TRT) [54] is the furthest component of the ID from the beam pipe, with a barrel region positioned at $563 < R < 1066$ mm and $|z| < 712$ mm and two end-caps at $644 < R < 1004$ mm and $848 < |z| < 2710$ mm. The method of detection used by the TRT differs from the previous ID modules: instead of using silicon semiconductors, the TRT consists of thin-walled proportional drift tubes called "straws" containing a nominal mixture of 70%/27%/3% xenon/carbon dioxide/oxygen gas.

In addition to being filled with this gas mixture, each straw contains a central gold-plated tungsten wire of diameter $32\text{ }\mu\text{m}$ and has a potential applied between the central wire and outer wall of the drift tubes. When charged particles pass through the straws, atoms within the gas are ionized and drift towards the walls of the straws while electrons drift towards the wire. The wire amplifies the signal of these electrons by a factor of approximately 20,000 by releasing an avalanche of electrons which creates an interpretable signal and allows the extraction of timing information.

Additional ionization can occur from transition radiation photons which originate from the thin material between straws made of polypropylene and polyethylene fibres. Incoming charged particles moving between media with differing refraction indexes have a probability of emitting these transition radiation photons with energies proportional to their Lorentz factor. This interaction is exploited during electron identification as electrons will have higher Lorentz factors (and therefore create a larger pulse within the wire) than many other charged particles such as muons and pions.

The TRT consists of 52,544 coaxial straws of length 144 cm in barrel region and 122,880 radial straws of length 37 cm in each end-cap, totalling almost 300,000 straws across the entire TRT. Due to these numbers and the geometry of ATLAS, charged particles are guaranteed to cross 35-40 straws in a pseudorapidity interval of $|\eta| < 2$. Overall, the TRT provides a hit resolution of $130\text{ }\mu\text{m}$ per straw [55].

3.2.4 The Calorimeters

Calorimeters are instruments that measure the energy of particles: incoming particles are absorbed by the calorimeter and deposit their full energy which is converted into a measurable signal. The calorimeter system within ATLAS uses two main types of calorimeters: electromagnetic calorimeters for energy measurements of electromagnetic particles, and hadronic calorimeters for energy measurements of hadronic particles. These calorimeters measure all SM particles excluding muons and neutrinos, with a coverage up to $|\eta| < 4.9$. The layout of these calorimeters within ATLAS can be seen in Figure 3.18.

The ATLAS calorimeters are *sampling* calorimeters which operate using an alternating pattern of layers of an absorber medium and an active medium. Incoming particles interact within the absorber medium which decreases their energy and creates a shower of secondary particles that subsequently interacts within the active medium to produce a detectable signal.

3.2.4.1 The Electromagnetic Calorimeter

The electromagnetic calorimeter or LAr calorimeter [57] has the primary function of measuring the energy of electrons and photons in the pseudorapidity region $|\eta| < 3.2$.

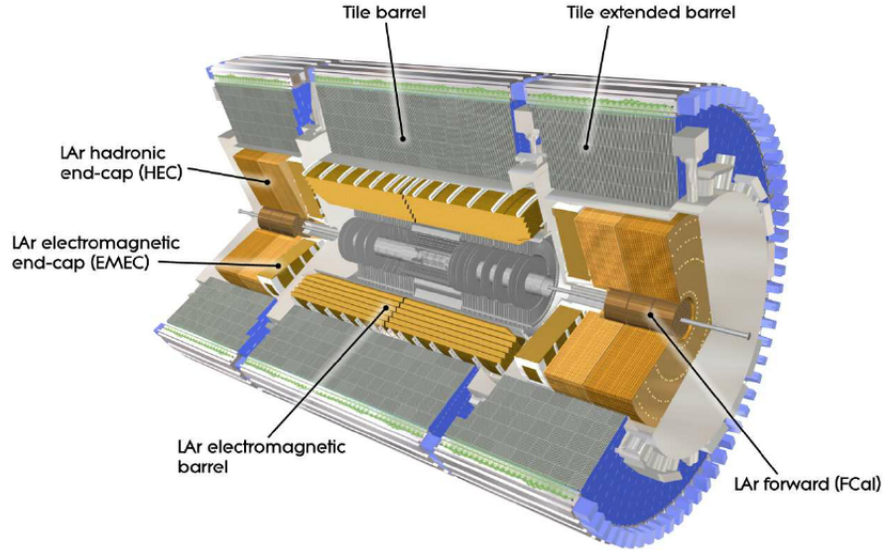


Figure 3.11: A figure displaying the arrangement of the electromagnetic and hadronic calorimeters within the ATLAS detector [56].

Lead is chosen as the absorber material, with liquid argon (LAr) as the active material. Two main processes occur within the lead absorber material that lead to showering and a measurement of incoming particle energy:

- *Bremsstrahlung*, where incoming electrons interact with the lead atoms' dense nucleus to lose kinetic energy which is emitted as bremsstrahlung photons.
- *Pair production*, where a photon is converted to an electron-positron pair.

Incoming particles will rapidly alternate between bremsstrahlung and pair production, depositing energy within the LAr active material each time. This process is called *showering*, and continues until the shower no longer has enough energy to produce further particles (i.e. the electron does not have enough kinetic energy to radiate as a photon or the photon no longer passes the energy threshold for electron-positron pair production). At this point, the particles continue losing their energy through more simple mechanisms until they come to a complete loss (via physical collisions with atoms for electrons and compton scattering/the photoelectric effect for photons).

These are not the only mechanisms through which EM particles can deposit energy within the EM calorimeter (for example pions are capable of producing a photon pair), however they are among the most common. It is important to note that muons also produce small energy deposits in the EM calorimeter, however due to the nature of muons as minimally ionising particles this is often simply the radiation of a low energy

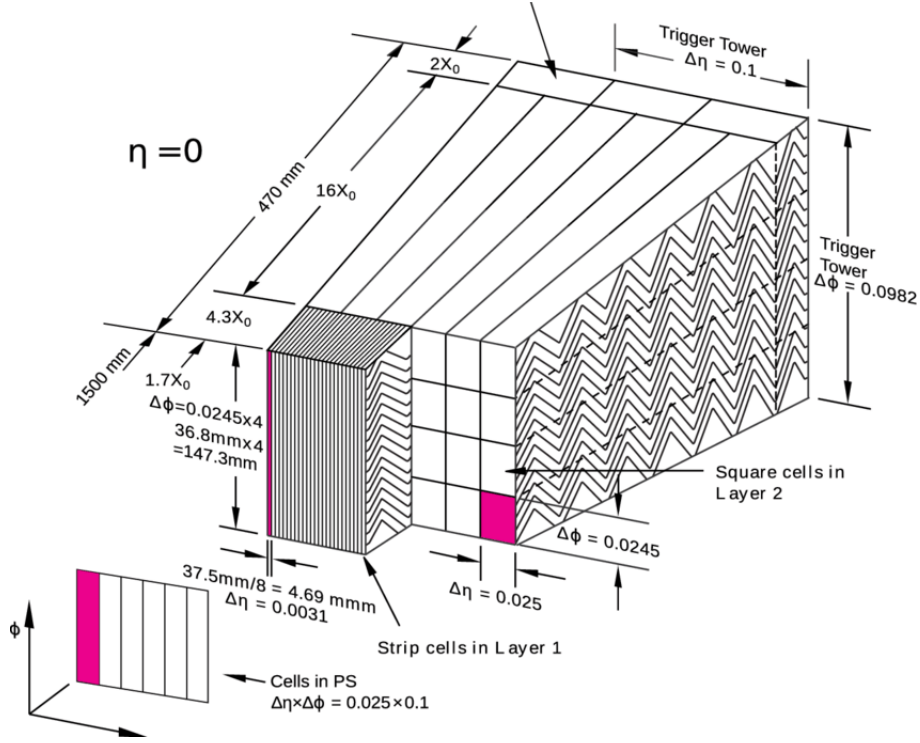


Figure 3.12: A figure showing the unique accordion shape of the ATLAS EM calorimeter [58].

photon. These low energy photons may shower and produce low energy showers, however these are often easily distinguishable from the higher energy showers of electrons and photons. Following the shower produced by an incoming particle, ionisation electrons within the LAr active material will drift towards a copper electrode (similarly to the system explained in 3.2.3.4) in order to produce a measurable signal.

The EM calorimeter consists of a barrel calorimeter providing coverage in the pseudorapidity range $0 < |\eta| < 1.475$ and two end-cap calorimeters providing coverage in the pseudorapidity range $1.375 < |\eta| < 3.2$. The geometry of the EM calorimeter uses a unique accordion-shaped geometry which allows for a completely hermetic design (i.e. no gaps of any kind are required between the absorber and active materials for devices such as readout systems). The readout of the EM calorimeter can occur from either the front or back, which allows for full coverage in ϕ . The accordion geometry of the EM calorimeter can be seen in Figure 3.12.

To perform the best possible energy measurement of an incoming particle, the particle must be completely stopped within the medium of the calorimeter. A greater calorimeter length increases the probability of completely stopping an incident particle, however additional length beyond what is required to stop the incident particle is inefficient in terms of maintenance, power, and cost. In order to find this ideal balance

of calorimeter length the radiation length, X_0 , is used to characterise the behaviour of the incident EM showers. X_0 is defined as the distance within a given material that an incident photon or electron must travel in order to lose $1/e$ of its energy. In total the EM calorimeter has a depth of over $22 X_0$ composed of three layers of varying depth, X_0 , and η/ϕ granularity plus an additional zeroth layer called the presampler [58].

These layers are:

The presampler (PS) layer, a relatively thin cluster of LAr layers only (i.e. no absorber material) separate from the calorimeter and positioned before some infrastructure components. The aim of the PS layer is to estimate the total loss of energy upstream of the calorimeter due to material interactions (within the inner detector, cryostat, and solenoid coil up to $|\eta| < 1.5$). The PS layer is only 11 mm thick in the barrel region and only 5 mm thick in the end-caps, covering a pseudorapidity range of $|\eta| < 1.8$.

Layer 1, which has a thickness of $4.4 X_0$ at $\eta = 0$ and is segmented into strips with varying granularity across η . For $|\eta| < 1.4$ and $1.5 < |\eta| < 2.4$ these are high granularity segmentation, whereas for the range of $1.4 < |\eta| < 1.5$ and $2.4 < |\eta| < 2.5$ the segmentation is coarser. The purpose of this differing granularity is to allow for discriminating power between photon showers caused by single photons, and showers from two collimated photons decaying from neutral hadrons (such as in the case of a neutral pion producing two photons). The cells in the finer granularity η region have the size of 0.003×0.0982 in $\Delta\eta \times \Delta\phi$, and the cells in the coarser η region have a size of 0.025×0.0982 in $\Delta\eta \times \Delta\phi$.

Layer 2, which has a thickness of $16 X_0$ where the bulk of energy depositing occurs. The cells in this layer have a size of 0.025×0.0245 in $\Delta\eta \times \Delta\phi$.

Layer 3, which has a thickness of $2 X_0$ designed to measure and correct for the leakage of higher energy calorimeter showers beyond the EM cal and potentially into the hadronic calorimeter. The cells in this layer have a size of 0.05×0.0245 in $\Delta\eta \times \Delta\phi$.

3.2.4.2 The Hadronic Calorimeter

Just as the EM calorimeter performs energy measurements of incoming EM particles, the hadronic calorimeter or Tile calorimeter [59] measures energies of incoming hadronic particles in the region of $|\eta| < 4.9$. The Tile calorimeter consists of three barrel layers and two wheels per end-cap, each using differing absorber and active materials:

- The barrel region uses plates of steel as its absorber material and plastic scintillator tiles as its active material.
- The hadronic end-cap (HEC) in the end-cap region $1.5 < |\eta| < 3.2$ uses copper as its absorber material and LAr as its active material.

Interactions with the steel nuclei in the barrel region cause particle showers containing charged particles that interact with the scintillating active material in order to produce ultraviolet scintillation photons. These photons are carried to photomultiplier tubes (PMTs) via wavelength shifting fibres which convert the photons into a measurable electronic signal. A larger interaction within the scintillation tiles produces a stronger signal, and so measuring the intensity of the signal allows for a measurement of energy deposited by the incident hadronic particle.

Hadronic showers are characterised by the *interaction length* which defined as the distance between interactions within a given material to reduce the number of relativistic charged particle by a factor of $1/e$. Hadronic showers occur via the strong interaction typically producing wider showers mainly consisting, allowing for coarser granularity than in the EM calorimeter.

The barrel region of the hadronic calorimeter has a depth of 9.7λ and cell sizes of 0.1×0.1 in $\Delta\eta \times \Delta\phi$ for the first two layers, and 0.2×0.1 in $\Delta\eta \times \Delta\phi$ in the last layer. The end-cap wheels have a depth of 10λ and similar granularity to the barrel region of 0.1×0.1 in $\Delta\eta \times \Delta\phi$ in the first wheel, and 0.2×0.1 in $\Delta\eta \times \Delta\phi$ for the second.

3.2.4.3 The Forward Calorimeter

ATLAS uses an additional calorimeter in the forward region of $3.2 < |\eta| < 4.9$ in order to increase the calorimeter coverage within ATLAS up to the pseudorapidity range of $|\eta| < 4.9$. The forward calorimeter (FCal) is a sampling calorimeter capable of performing energy measurements of both EM and hadronic particles via its use of a combination of multiple absorber materials.

The FCal has a depth of 10λ and is segmented into three layers: while the FCal consistently uses LAr as its active material, the first layer uses copper layers as its absorber material in order to perform measurements of EM particles before switching to a tungsten absorber material in the second and third layers for hadronic energy measurements.

3.2.5 The Muon Spectrometer

The final and outermost subsystem of the ATLAS detector is the Muon Spectrometer (MS) [60]. Interspersed between the toroidal magnet, the muon system is composed of

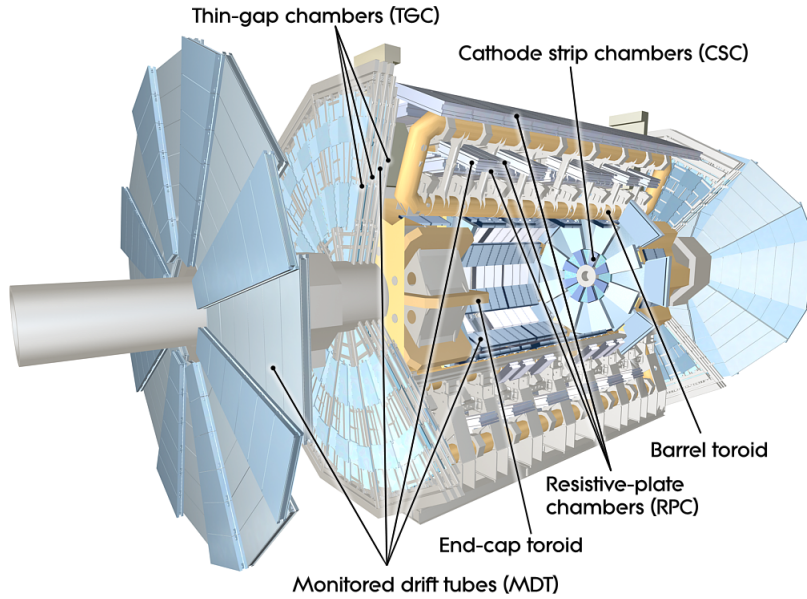


Figure 3.13: A figure showing the position of the individual muon systems within ATLAS [42].

two systems made up of pairs of triggering and tracking systems with the aim to track and measure muons in the pseudorapidity range of $|\eta| < 2.7$. Muons that pass through the system are subjected to ATLAS' magnetic field (discussed in Section 3.2.2), bending the muon tracks and allowing for muon momentum measurements.

The MS can be divided into a barrel region in the pseudorapidity range of $|\eta| < 1.05$ and an end-cap region from $1.05 < |\eta| < 2.7$. Four main components in various configurations are used to provide the full functionality of the MS: [Monitored Drift Tubes \(MDTs\)](#) [61], [Resistive Plate Chambers \(RPCs\)](#) [62], [Cathode Strip Chambers \(CSCs\)](#) [63], and [Thin Gap Chambers \(TGCs\)](#) [64]. The positioning of each of these components can be seen in Figure 3.19.

Monitored Drift Tubes (MDTs)

MDTs can essentially be thought of as larger versions of the TRT straws discussed in Section 3.2.3.4. They are drift tubes with a diameter of 3 cm containing a central wire made of tungsten and filled with argon gas, subjected to a potential between the tube wall and the wire. Muons ionise the argon gas within the MDTs, and the electrons drift towards the tungsten wire to produce a detectable signal. The drift time of the charge within the MDTs allows for attainment of a spatial precision of $80 \mu\text{m}$.

Resistive Plate Chambers (RPCs)

A single RPC unit contains two gas volumes bounded by two bakelite capacitor plates

and separated by a grid of 2 mm spacers. The gas volume is filled with $\text{C}_2\text{H}_2\text{F}_4$ gas and subjected to a potential. Muons passed through the gas volume ionise the gas, and ionised electrons from these interactions are read out from the RPC unit allowing for a trigger timing resolution of 2 nanoseconds.

Cathode Strip Chambers (CSCs)

CSCs are multi-wire proportional chambers, which typically consist of equally spaced parallel wires sandwiched between cathode planes [65]. The remaining unit volume is filled with gas, which is ionised by incident charged particles. The CSCs uses alternating planes of tungsten wires and two segmented cathodes in a 80%/20% argon/carbon dioxide gas volume, with one set of cathode strips running perpendicular to the wires and the other set of strips running parallel to the wires. This configuration of the CSCs provides a resolution of 60 μm per layer.

Thin Gap Chambers (TGCs)

Much like the CSCs, the TGCs are also multi-wire proportional chambers. The key difference between the two is their slightly differing design: the TGCs use 50 μm gold plated tungsten wires and a 45%/55% n-pentane/carbon dioxide gas volume [66]. The TGCs allow for a faster timing resolution than the CSCs alone (approximately 4 ns compared with 7 ns).

The MS barrel uses a combination of MDTs and RPCs for tracking and triggering respectively. The barrel component of the MS consists of three cylindrical layers of MDTs, with RPCs surrounding the last two MDT layers. The end-cap region of the MS consists of four wheels containing MDTs and CSCs for tracking, and TGCs for triggering: the first wheel at higher pseudorapidity of $2.5 < |\eta| < 2.7$ uses CSCs in place of MDTs, as the occupancy of the MDTs is too high in this region. The remaining three wheels use MDTs, with three layers of TGCs surrounding the third wheel. The arrangement of the muon system can be seen in Figure 3.14.

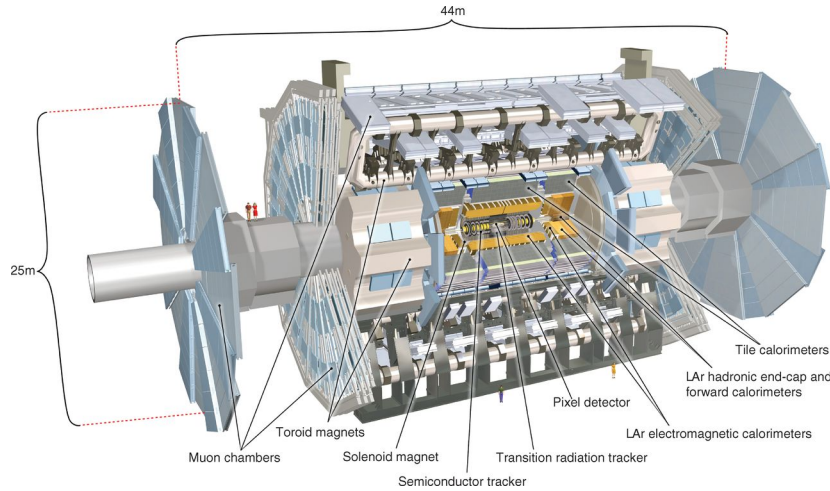


Figure 3.15: A figure showing the subsystems of the ATLAS detector [42].

The ATLAS detector operates using a combination of several subsystems, each of which can be seen in Figure 3.15.

These subsystems are layered outwards from the central interaction points, largely in the form of concentric cylinders (however this is not true for every component which will be discussed in the following sections). These systems can be organised into four categories based on their function: the magnet system, the inner detector, the calorimeter system, and the muon system. Together with the trigger system, these components are designed to allow ATLAS to operate with the highest possible efficiency.

3.3.1 Magnet System

The ATLAS magnet system consists of four magnets: a single solenoid magnet, and three toroidal magnets (which contribute an important part of the ATLAS name). The central solenoid provides the magnetic field for the inner detector, and the toroidal magnets provide the magnetic field for the muon system.

The solenoid magnet is named the Central Solenoid Magnet and serves the purpose of bending the path of charged particles within the inner detector so that their momentum may be measured. The most important function of this system for this analysis is the 2T axial magnetic field that it exerts within ATLAS. The magnet weighs 5 tonnes, and is aligned with the z-axis of the beam pipe. The solenoid magnet is also capable of storing a total of 38MJ of energy.

The toroidal magnets have different designs for their varying purposes. The first is the end-cap magnets: large, doughnut shaped magnets that rest at either end of the detector and provide the magnetic field in the end-cap regions of the muon system. The second is the barrel toroid - longer, 25.3m toroidal coils that span the length of the

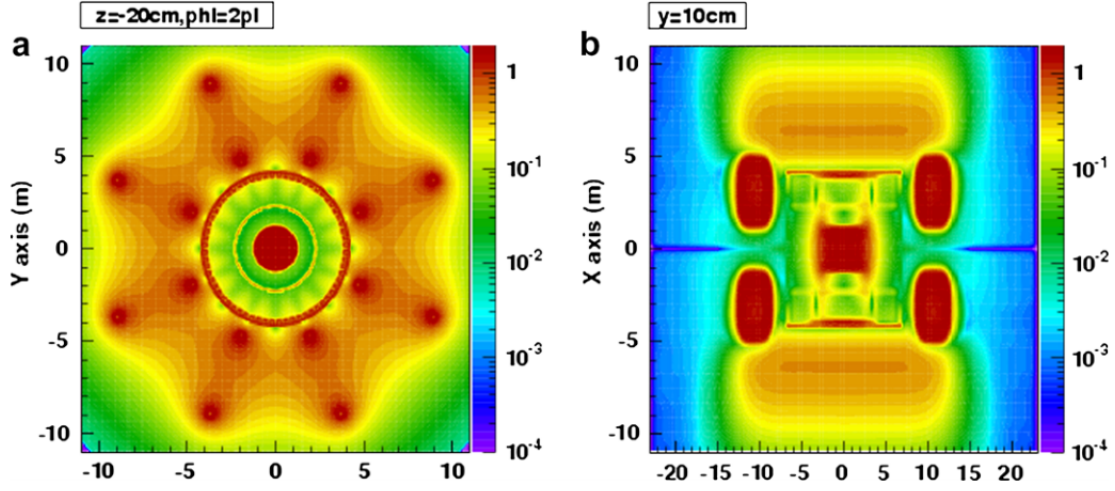


Figure 3.16: The shape of the magnetic field within the ATLAS detector [47].

muon system and provide a constant toroidal magnetic field to that system. The contributions of the barrel and end-cap toroids to the toroidal field around the muon detectors is as follows: 0.5T from the barrel toroid, and 1T from each of the end-cap toroids. Each end-cap magnet weighs 240 tonnes and stores 0.25GJ of energy. The barrel toroid consists of eight individual coils stored within vacuum vessels that surround both the end-cap magnets and the calorimeter systems. The barrel toroid weighs a total of 830 tonnes, and stores a total of 1.08GJ of energy. The shape of the ATLAS magnetic field can be seen in Figure 3.16. [40–42]

3.3.2 Inner Detector

The inner detector is the most central component of ATLAS and makes the most immediate measurements after a collision such as those of the primary and secondary vertex, and of particle momentum. The inner detector covers a pseudorapidity range of $|\eta| < 2.5$ and consists of the Pixel Detector, Semiconductor Tracker (SCT), and the Transition Radiation Tracker (TRT). These components can be seen in Figure 3.17.

Both the pixel detector and SCT consist of thousands of silicon sensors. The pixel detector consists of 1744 silicon wafers (each 250 μm thick), and the SCT of 15912 silicon wafers (each $285 \pm 15 \mu\text{m}$ thick). The charged particles that pass through the pixel detector and SCT ionise within the submodules' silicon semiconductors, freeing electrons from atoms within the silicon and creating ion-electron pairs. By interpreting the resultant signal created at the points within these wafers that these ion-electron pairs are created, the path of the charged particles that pass through the inner detector can be measured [40–42].

The inner detector performs several crucial functions within ATLAS: By performing measurements of charged particles that pass through the inner detector as their paths are bent by the magnet system, the inner detector can perform preliminary momentum measurements and track the paths of these charged particles throughout ATLAS. The measurements of momentum performed by the inner detector are supplemented by readings from other detector subsystems (such as energy deposits in the calorimeters), however the inner detector performs the most precise measurement of muon momentum. The paths measured by the inner detector provide excellent measurements of the tracks of charged particles, and are crucial for reconstructing events within ATLAS as they allow the detector triggers to correlate particle tracks to hits in other detector systems. By mapping hits in other detector subsystems with the paths tracked by the inner detector, it is possible to identify the kinematics and flavour of each particle travelling through ATLAS in order to fully describe each event. The inner detector is also responsible for identifying the main interaction point of each collision, by tracing the particle tracks back to the point where they originate.

The number of particle tracks that occur within each event is very high, and in order to perform these measurements the inner detector must have a very high spatial resolution. The pixel detector and SCT have spatial resolutions of $12\mu\text{m}$ and $16\mu\text{m}$ respectively, which is essential to allow the detector to discern between the tracks of charged particles within the inner detector. The large number of events that occur within ATLAS every second can only be measured if the detector is able to accurately measure each involved particle, hence being able to distinguish each event's tracks and collision points is essential to all measurements performed by ATLAS.

As charged particles pass through the TRT, they pass through drift tubes filled with a mixture of xenon, carbon dioxide, and oxygen gas. The charged particles emit transition radiation as they pass from the detector material into the gas, and also ionise the gas as they travel through it. The number of photons produced via transition radiation and electrons produced from EM-ionisation can be used to help distinguish between charged particles such as electrons and pions. By observing which of the drift tubes detected a signal, the TRT can supplement the measurement of the path of the charged particle performed by the pixel detector and SCT.

3.3.3 Calorimeter System

Two different calorimeters surround the inner detector and solenoid magnet to continue the measurements of particles travelling through ATLAS: the Electromagnetic Calorimeter and Hadronic Calorimeter (each of which consists of multiple pieces). The ATLAS calorimeters are sampling calorimeters, meaning that they work via a combination of absorber (or sampling) materials which cause an interaction within the module, and an active material which produces a signal which is interpreted by ATLAS. The electromagnetic calorimeter consists of lead absorbers with a liquid argon (LAr)

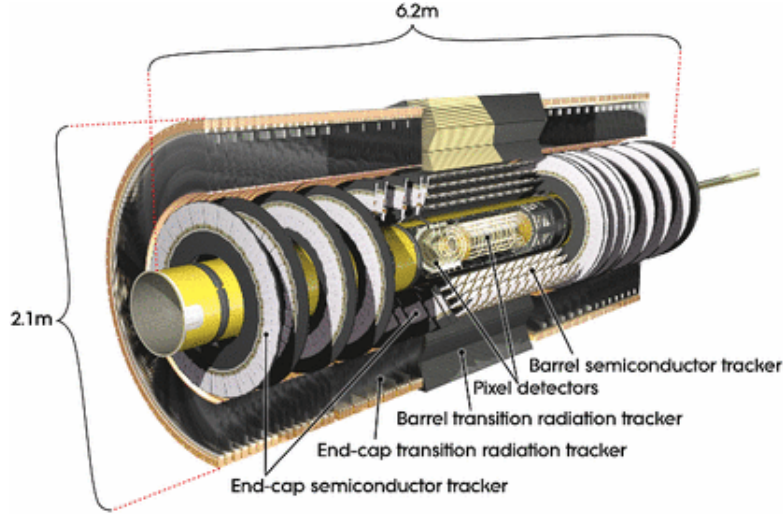


Figure 3.17: A figure showing the layout of the inner detector within ATLAS [42].

activate material, and the hadronic calorimeter consists of steel absorbers with scintillators as the active material. The layout of the calorimeter system can be seen in Figure 3.18.

By working in tandem, the two calorimeters perform measurements of the energy deposited by the travelling particles, regardless of whether the particles are charged or neutral. Naturally, the electromagnetic calorimeter focuses on absorbing the energy produced in electromagnetic showers, and the Hadronic calorimeter absorbs energy from hadronic showers. Both calorimeters surround the beam pipe, fully covering the azimuthal angle ϕ . Each calorimeter system is a combined effort from several pieces in order to cover a large range of $|\eta| < 4.9$.

In order to allow ATLAS to operate at maximum efficiency, incoming particles that cause electromagnetic and hadronic showers need to be fully contained within the calorimeters. This ensures that ATLAS can study the full shower, and prevents particles other than muons from penetrating through to the muon system. This is achieved by constructing the calorimeters to be an appropriate depth: the EM calorimeter is designed to be between 24 and 27 radiation lengths (X_0) deep, and the hadronic calorimeter is designed to be 10 nuclear interaction lengths (λ) thick. X_0 and λ represent the differing manners in which EM and hadronic particles lose energy, and for each unit one radiation/interaction length is the distance at which a travelling particle decreases to $1/e$ of its original energy.

The electromagnetic calorimeter consists of three parts: a barrel calorimeter and two end-cap calorimeters, with the barrel calorimeter covering $0 < |\eta| < 1.475$ and the end-cap calorimeters covering $1.375 < |\eta| < 3.2$. All of these calorimeters follow the geometry of an accordion, allowing full coverage of ϕ within the EM calorimeter without

any spaces [40–42].

EM particles passing through the EM calorimeter interact with lead absorbers, creating a shower of lower energy particles. The incoming particles produce photons via the bremsstrahlung process (or other means such as a pion producing two photons), which then produce additional electrons via pair production. This alternating process of emitting photons which then produce electrons continues until the total energy of the shower is below that required for pair production to occur. Muons are capable of radiating photons as they pass through the EM calorimeter, which may produce additional secondary objects themselves. Typically these jets will be far less energetic than those produced by incoming electrons and photons, as photons radiated by muons carry only a small portion of the incident muon’s energy.

The EM calorimeter is fine-granulated, so that the calorimeter can reconstruct each showering particle. EM showers can easily have many simultaneous interactions (such as a pion decaying into two photons within proximity of an additional photon), and it is important to be able to distinguish between these occurrences for a detailed analysis.

Once these incident particles have lost enough energy to be beneath the energy requirement to produce an EM shower, energy loss mainly occurs by ionisation of the LAr within the EM calorimeter which frees additional electrons. The electrons produced within the LAr are attracted toward a copper electrode where they are interpreted into an electronic signal which reveals the amount of energy deposited by the original incident EM particle. Within the EM calorimeter, the thickness is $> 22 X_0$ thick in the barrel calorimeters and $> 24 X_0$ in the end-cap calorimeters.

The hadronic calorimeter is similarly consisting of three distinct parts: the hadronic tile calorimeter, LAr forward calorimeter (FCal), and the LAr hadronic end-caps (HEC). One large central barrel cylinder and two smaller extended barrel cylinders make up the tile calorimeter - a system of alternating steel absorbers and scintillating plates.

Travelling hadrons interact with the nuclei of the steel absorbers, producing additional particles. These particles then continue to interact, producing large showers of interactions. As these showers continue into the hadronic calorimeter, charged particles produce photons within the scintillating material. The photons emitted are carried to photomultiplier tubes via wavelength shifting fibres, where the photomultiplier tubes (PMTs) convert the photons into an electronic signal. By measuring the intensity of the light that creates the electronic signal, the energy deposited by the travelling hadron can be measured. The barrel tile calorimeter has a total thickness of 9.7λ for the combination of both the central barrel cylinder and extended barrel cylinders [40–42].

In order to be able to accurately measure the energy of incoming particles, the barrel calorimeter is required to have a high energy resolution (σ/E). In an event where energy is deposited within a calorimeter, a calorimeter with high energy efficiency is better equipped to reconstruct the energy of the original event (and therefore high energy resolution was an important factor considered during the design of ATLAS). Using

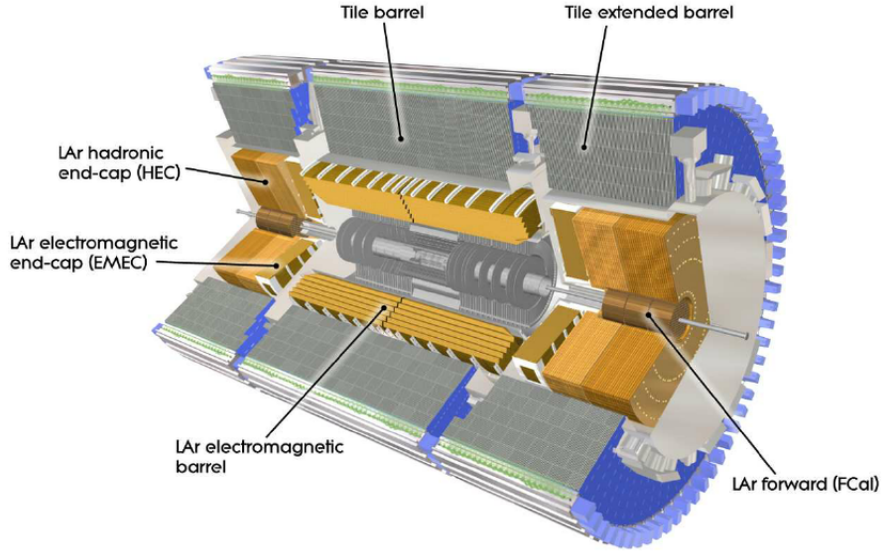


Figure 3.18: A figure displaying the arrangement of the electromagnetic and hadronic calorimeters within the ATLAS detector [42].

electron test beam measurements, the energy resolution of the EM barrel calorimeter was found to be $\sigma/E = 10\%/\sqrt{E} \oplus 2\%$ (where the simple \oplus represents a quadratic sum) [68].

In addition to the barrel tile calorimeter which covers a range of $0 < |\eta| < 1.0$ are the HEC and the FCal, which maximise the η coverage of the calorimeters. The FCal is positioned in the very far forward and backward regions of $3.1 < |\eta| < 4.9$. The FCal consists of three modules, each containing a layer of a metal absorber and electrodes, plus LAr as the active detecting material. The first module is made of copper in order to allow electromagnetic measurements, and the other two layers are made of tungsten to allow measurements of hadronic interactions in the same method as the tile calorimeter. The total depth of the FCal is 10 interaction lengths.

The HEC overlaps with the tile calorimeter and the FCal in order to ensure full coverage. The HEC uses copper as its absorber and LAr as its active material, covering a range of $1.5 < |\eta| < 3.2$. Together these three pieces form the hadronic calorimeter and cover the pseudorapidity range of $0 < |\eta| < 4.9$. In test beam studies, the energy resolution of hadrons in the tile calorimeter was measured to be $\sigma/E = 52.9\%/\sqrt{E} \oplus 5.7\%$ [69].

3.3.4 Muon System

The final ATLAS detector subsystem is the muon system which rests outside the calorimeter system and inner detector. The muon system's role is to measure the path

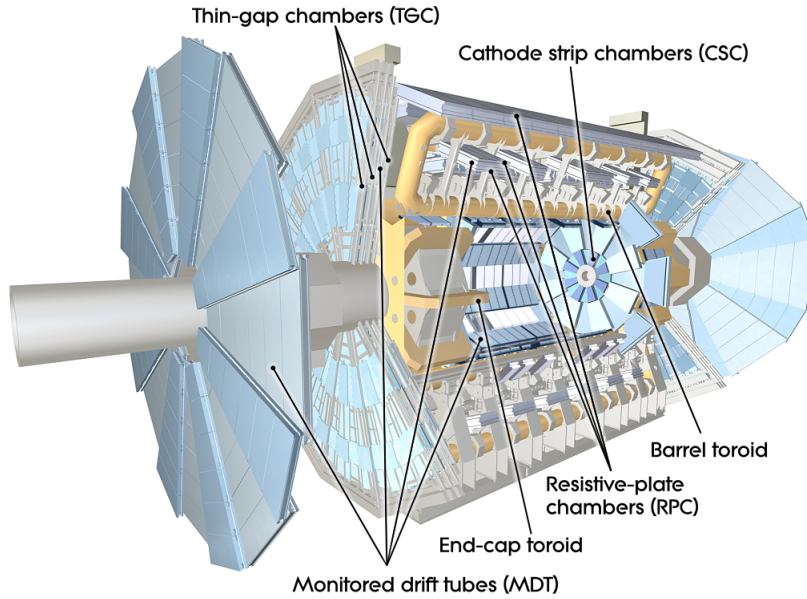


Figure 3.19: A figure showing the position of the individual muon systems within ATLAS [42].

and momentum of muons in the pseudorapidity range of $|\eta| < 2.7$. The measurements in this region are dependent upon the toroidal magnets, which allow the tracks of charged particles able to penetrate the other detector systems to be measured. The barrel toroid provides the magnetic field in the region $|\eta| < 1.4$, the end-cap toroids provide the field in the region $1.6 < |\eta| < 2.7$, and the two work in tandem to produce the field in the transition region of $1.4 < |\eta| < 1.6$.

The bending of the muon tracks allows for measurements to be made in a similar fashion as to within the inner detector, and this is coupled with additional measurements from four components: precision measurements from monitored drift tubes (MDT) and cathode strip chambers (CSC), and trigger measurements from resistive plate chambers (RPC) and thin gap chambers (TGC).

The CSCs are located in the forward regions of $2 < |\eta| < 2.7$, as they are capable of dealing with the highest particle fluxes of up to 1000 Hz cm^{-2} . The MDTs are located cover the region $|\eta| < 2.7$ and consist of layers of drift tubes: cylinders containing a mixture of argon and carbon dioxide gas, with a wire at the centre. Muons that travel through the drift tubes ionise the gas and produce electrons and ions which drift to the wire and edge of the drift tube respectively, and are interpreted as an electronic signal. By observing the amount of ionisation, particle drift time, and the time and position of each emitted signal, the momentum of the travelling muon can be measured. The layout of the muon system can be seen in Figure 3.19.

The RPCs and TGCs serve as fast trigger chambers, able to provide track information

approximately 10ns after a particle penetrates. The RPCs are located in the barrel covering the range $|\eta| < 1.05$, and the TGCs in the end-cap covering the region $1.05 < |\eta| < 2.4$. While the CSCs and MDTs record precision measurements regarding the incident muons, the RPCs and TGCs are utilised for providing information to the trigger systems.

The RPCs are gaseous parallel electrode-plate detectors consisting of two resistive plates separated by a 2mm gas gap: incoming muons are deflected towards the anode of the RPC allowing for a signal readout. TPCs are multi-wire proportional chambers arranged into layers positioned around the MDTs and in front of the most inward positioned tracking layer. As incident muons penetrate the sub layers within the TPCs, a signal is emitted if a muon is detected in multiple layers of the detector. The time and position of where this signal originates corresponds to a muon hit, and aids the trigger system in identifying muon events [40–42].

3.3.5 Trigger System

The trigger system’s function is to manage the enormous number of collisions that occur within ATLAS every second, identifying events that correspond to the expected standards of ATLAS, and ignoring those that do not. This operation is performed by a combination of a hardware based Level 1 (L1) trigger and a software based High Level Trigger (HLT).

The L1 trigger uses information from the calorimeters and muon system to identify regions of interest within the recorded data, and performs the first classification of the data recorded, before passing events are sent to the HLT. This operation takes place within $2.5\mu\text{s}$, and reduces the event rate from 40MHz to less than 75kHz (although it is still possible to operate with up to 100kHz output rate from the L1 trigger).

The HLT runs on a dedicated server farm, and uses high speed algorithms to further refine events in the region of interest that pass the L1 trigger. The HLT reduces the event rate further to 1kHz, processing each event in an average of 0.2s.

References

- [1] P. Nason, S. Dawson, and R. Keith Ellis. The One Particle Inclusive Differential Cross-Section for Heavy Quark Production in Hadronic Collisions. *Nucl. Phys.*, B327:49, 1989. [Erratum: Nucl. Phys.B335,260(1990)], URL [http://dx.doi.org/10.1016/0550-3213\(90\)90180-L](http://dx.doi.org/10.1016/0550-3213(90)90180-L), [10.1016/0550-3213\(89\)90286-1](http://dx.doi.org/10.1016/0550-3213(89)90286-1).
- [2] John M. Campbell, R. Keith Ellis, F. Maltoni, et al. Associated production of a Z

- Boson and a single heavy quark jet. *Phys. Rev.*, D69:074021, 2004. [hep-ph/0312024](http://dx.doi.org/10.1103/PhysRevD.69.074021), URL <http://dx.doi.org/10.1103/PhysRevD.69.074021>.
- [3] John M. Campbell, R. Keith Ellis, F. Maltoni, et al. Production of a Z boson and two jets with one heavy-quark tag. *Phys. Rev.*, D73:054007, 2006. [Erratum: *Phys. Rev.* D77,019903(2008)], [hep-ph/0510362](http://dx.doi.org/10.1103/PhysRevD.77.019903), URL <http://dx.doi.org/10.1103/PhysRevD.77.019903>, [10.1103/PhysRevD.73.054007](http://dx.doi.org/10.1103/PhysRevD.73.054007).
- [4] Fernando Febres Cordero, L. Reina, and D. Wackeroth. W- and Z-boson production with a massive bottom-quark pair at the Large Hadron Collider. *Phys. Rev.*, D80:034015, 2009. [0906.1923](http://dx.doi.org/10.1103/PhysRevD.80.034015), URL <http://dx.doi.org/10.1103/PhysRevD.80.034015>.
- [5] Georges Aad et al. (ATLAS). Measurement of differential production cross-sections for a Z boson in association with b -jets in 7 TeV proton-proton collisions with the ATLAS detector. *JHEP*, 10:141, 2014. [1407.3643](http://dx.doi.org/10.1007/JHEP10(2014)141), URL [http://dx.doi.org/10.1007/JHEP10\(2014\)141](http://dx.doi.org/10.1007/JHEP10(2014)141).
- [6] Serguei Chatrchyan et al. (CMS). Inclusive b -jet production in pp collisions at $\sqrt{s} = 7$ TeV. *JHEP*, 04:084, 2012. [1202.4617](http://dx.doi.org/10.1007/JHEP04(2012)084), URL [http://dx.doi.org/10.1007/JHEP04\(2012\)084](http://dx.doi.org/10.1007/JHEP04(2012)084).
- [7] M. Tanabashi, K. Hagiwara, K. Hikasa, et al. (Particle Data Group). Review of Particle Physics. *Phys. Rev. D*, 98:030001, Aug 2018. URL <http://dx.doi.org/10.1103/PhysRevD.98.030001>.
- [8] Fabio Maltoni, Giovanni Ridolfi, and Maria Ubiali. b -initiated processes at the LHC: a reappraisal. *JHEP*, 07:022, 2012. [Erratum: *JHEP*04,095(2013)], [1203.6393](http://dx.doi.org/10.1007/JHEP04(2013)095), URL [http://dx.doi.org/10.1007/JHEP04\(2013\)095](http://dx.doi.org/10.1007/JHEP04(2013)095), [10.1007/JHEP07\(2012\)022](http://dx.doi.org/10.1007/JHEP07(2012)022).
- [9] Juan Rojo. PDF4LHC recommendations for Run II. *PoS*, DIS2016:018, 2016. [1606.08243](http://dx.doi.org/10.1007/JHEP04(2013)095).
- [10] Georges Aad et al. (ATLAS Collaboration) (ATLAS). Observation of a new particle in the search for the Standard Model Higgs boson with the ATLAS detector at the LHC. *Phys. Lett.*, B716:1, 2012. [1207.7214](http://dx.doi.org/10.1016/j.physletb.2012.08.020), URL <http://dx.doi.org/10.1016/j.physletb.2012.08.020>.
- [11] Serguei Chatrchyan et al. (CMS Collaboration) (CMS). Observation of a new boson at a mass of 125 GeV with the CMS experiment at the LHC. *Phys. Lett.*, B716:30, 2012. [1207.7235](http://dx.doi.org/10.1016/j.physletb.2012.08.021), URL <http://dx.doi.org/10.1016/j.physletb.2012.08.021>.
- [12] Guido Altarelli. A QCD primer. *AIP Conf. Proc.*, 631(1):70, 2002. [hep-ph/0204179](http://dx.doi.org/10.1063/1.1513677), URL <http://dx.doi.org/10.1063/1.1513677>.

- [13] F. Englert and R. Brout. Broken Symmetry and the Mass of Gauge Vector Mesons. *Phys. Rev. Lett.*, 13:321, Aug 1964. URL <http://dx.doi.org/10.1103/PhysRevLett.13.321>.
- [14] Peter W. Higgs. Broken Symmetries and the Masses of Gauge Bosons. *Phys. Rev. Lett.*, 13:508, Oct 1964. URL <http://dx.doi.org/10.1103/PhysRevLett.13.508>.
- [15] Sidney D. Drell and Tung-Mow Yan. Massive Lepton-Pair Production in Hadron-Hadron Collisions at High Energies. *Phys. Rev. Lett.*, 25:316, Aug 1970. URL <http://dx.doi.org/10.1103/PhysRevLett.25.316>.
- [16] A. D. Martin, W. J. Stirling, R. S. Thorne, et al. Parton distributions for the LHC. *Eur. Phys. J.*, C63:189, 2009. 0901.0002, URL <http://dx.doi.org/10.1140/epjc/s10052-009-1072-5>.
- [17] Oliver Sim Brüning, Paul Collier, P Lebrun, et al. *LHC Design Report*. CERN Yellow Reports: Monographs. CERN, Geneva, 2004. URL <http://dx.doi.org/10.5170/CERN-2004-003-V-1>.
- [18] Oliver Sim Brüning, Paul Collier, P Lebrun, et al. *LHC Design Report*. CERN Yellow Reports: Monographs. CERN, Geneva, 2004. URL <http://dx.doi.org/10.5170/CERN-2004-003-V-2>.
- [19] Michael Benedikt, Paul Collier, V Mertens, et al. *LHC Design Report*. CERN Yellow Reports: Monographs. CERN, Geneva, 2004. URL <http://dx.doi.org/10.5170/CERN-2004-003-V-3>.
- [20] L Arnaudon, P Baudrenghien, M Baylac, et al. Linac4 Technical Design Report. Technical Report CERN-AB-2006-084. CARE-Note-2006-022-HIPPI, CERN, Geneva, Dec 2006. Revised version submitted on 2006-12-14 09:00:40, URL <https://cds.cern.ch/record/1004186>.
- [21] G. Arnison, A. Astbury, B. Aubert, et al. Experimental observation of isolated large transverse energy electrons with associated missing energy at $s=540$ GeV. *Physics Letters B*, 122(1):103, 1983. URL [http://dx.doi.org/https://doi.org/10.1016/0370-2693\(83\)91177-2](http://dx.doi.org/https://doi.org/10.1016/0370-2693(83)91177-2).
- [22] G. Arnison, A. Astbury, B. Aubert, et al. Experimental observation of lepton pairs of invariant mass around 95 GeV/c² at the CERN SPS collider. *Physics Letters B*, 126(5):398, 1983. URL [http://dx.doi.org/https://doi.org/10.1016/0370-2693\(83\)90188-0](http://dx.doi.org/https://doi.org/10.1016/0370-2693(83)90188-0).
- [23] Christiane Lefèvre. The CERN accelerator complex. Complexe des accélérateurs du CERN, Dec 2008. URL <https://cds.cern.ch/record/1260465>.

- [24] R. Assmann, M. Lamont, and S. Myers. A brief history of the LEP collider. *Nucl. Phys. B Proc. Suppl.*, 109:17, 2002. URL [http://dx.doi.org/10.1016/S0920-5632\(02\)90005-8](http://dx.doi.org/10.1016/S0920-5632(02)90005-8).
- [25] *LEP design report*. CERN, Geneva, 1983. By the LEP Injector Study Group, URL <https://cds.cern.ch/record/98881>.
- [26] *LEP design report*. CERN, Geneva, 1984. Copies shelved as reports in LEP, PS and SPS libraries, URL <https://cds.cern.ch/record/102083>.
- [27] Carlo Wyss. *LEP design report, v.3: LEP2*. CERN, Geneva, 1996. Vol. 1-2 publ. in 1983-84, URL <https://cds.cern.ch/record/314187>.
- [28] V Parma and L Rossi. Performance of the LHC magnet system. (CERN-ATS-2009-023):6 p, Sep 2009. URL <https://cds.cern.ch/record/1204578>.
- [29] The ATLAS Collaboration, G Aad, E Abat, et al. The ATLAS Experiment at the CERN Large Hadron Collider. *Journal of Instrumentation*, 3(08):S08003, aug 2008. URL <http://dx.doi.org/10.1088/1748-0221/3/08/s08003>.
- [30] The CMS Collaboration, S Chatrchyan, G Hmayakyan, et al. The CMS experiment at the CERN LHC. *Journal of Instrumentation*, 3(08):S08004, aug 2008. URL <http://dx.doi.org/10.1088/1748-0221/3/08/s08004>.
- [31] The ALICE Collaboration, K Aamodt, A Abrahantes Quintana, et al. The ALICE experiment at the CERN LHC. *Journal of Instrumentation*, 3(08):S08002, aug 2008. URL <http://dx.doi.org/10.1088/1748-0221/3/08/s08002>.
- [32] The LHCb Collaboration, A Augusto Alves, L M Andrade Filho, et al. The LHCb Detector at the LHC. *Journal of Instrumentation*, 3(08):S08005, aug 2008. URL <http://dx.doi.org/10.1088/1748-0221/3/08/s08005>.
- [33] Lyndon Evans and Philip Bryant. LHC Machine. *Journal of Instrumentation*, 3(08):S08001, aug 2008. URL <http://dx.doi.org/10.1088/1748-0221/3/08/s08001>.
- [34] G Robert-Démolaize. Design and Performance Optimization of the LHC Collimation System, 2006. Presented on 20 Nov 2006, URL <https://cds.cern.ch/record/1004869>.
- [35] Stefano Redaelli. Beam Cleaning and Collimation Systems. 08 2016. URL <http://dx.doi.org/10.5170/CERN-2016-002.403>.

- [36] Daniel Boussard and Trevor Paul R Linnecar. The LHC Superconducting RF System. Technical Report LHC-Project-Report-316. CERN-LHC-Project-Report-316, CERN, Geneva, Dec 1999. URL <https://cds.cern.ch/record/410377>.
- [37] R Bailey and Paul Collier. Standard Filling Schemes for Various LHC Operation Modes. Technical Report LHC-PROJECT-NOTE-323, CERN, Geneva, Sep 2003. URL <https://cds.cern.ch/record/691782>.
- [38] B G Taylor (RD12 Collaboration). Timing distribution at the LHC. 2002. URL <http://dx.doi.org/10.5170/CERN-2002-003.63>.
- [39] Richard Hawkings Eric Torrence. ATLAS Public Luminosity Results for Run 2, 2020. URL <https://twiki.cern.ch/twiki/bin/view/AtlasPublic/LuminosityPublicResultsRun2>.
- [40] A. Airapetian et al. (ATLAS). ATLAS: Detector and physics performance technical design report. Volume 1. 1999.
- [41] A. Airapetian et al. (ATLAS). ATLAS: Detector and physics performance technical design report. Volume 2. 1999.
- [42] G. Aad et al. (ATLAS). The ATLAS Experiment at the CERN Large Hadron Collider. *JINST*, 3:S08003, 2008. URL <http://dx.doi.org/10.1088/1748-0221/3/08/S08003>.
- [43] A Yamamoto, T Kondo, Y Doi, et al. Design and development of the ATLAS central solenoid magnet. *IEEE Trans. Appl. Supercond.*, 9(KEK-98-192. 2, pt.1):852, Nov 1998. URL <http://dx.doi.org/10.1109/77.783430>.
- [44] J P Badiou, J Beltramelli, J M Baze, et al. (ATLAS Collaboration). *ATLAS barrel toroid: Technical Design Report*. Technical design report. ATLAS. CERN, Geneva, 1997. Electronic version not available, URL <http://cds.cern.ch/record/331065>.
- [45] *ATLAS end-cap toroids: Technical Design Report*. Technical design report. ATLAS. CERN, Geneva, 1997. Electronic version not available, URL <http://cds.cern.ch/record/331066>.
- [46] J.J. Goodson. Search for Supersymmetry in States with Large Missing Transverse Momentum and Three Leptons including a Z-Boson. Ph.D. thesis, Stony Brook University, May 2012. Presented 17 Apr 2012.
- [47] H.H.J. ten Kate. The ATLAS superconducting magnet system at the Large Hadron Collider. *Physica C: Superconductivity*, 468(15):2137, 2008. Proceedings of the 20th International Symposium on Superconductivity (ISS 2007), URL <http://dx.doi.org/https://doi.org/10.1016/j.physc.2008.05.146>.

- [48] *ATLAS inner detector: Technical Design Report, 1*. Technical design report. ATLAS. CERN, Geneva, 1997. URL <https://cds.cern.ch/record/331063>.
- [49] S Haywood, L Rossi, R Nickerson, et al. (ATLAS Collaboration). *ATLAS inner detector: Technical Design Report, 2*. Technical design report. ATLAS. CERN, Geneva, 1997. URL <https://cds.cern.ch/record/331064>.
- [50] Joao Pequeno. Computer generated image of the ATLAS inner detector, Mar 2008. URL <https://cds.cern.ch/record/1095926>.
- [51] M Capeans, G Darbo, K Einsweiler, et al. (ATLAS Collaboration). ATLAS Insertable B-Layer Technical Design Report. Technical Report CERN-LHCC-2010-013. ATLAS-TDR-19, Sep 2010. URL <https://cds.cern.ch/record/1291633>.
- [52] Beniamino Di Girolamo. ATLAS Pixel. *PoS, Vertex 2011:006*, 2012. URL <http://dx.doi.org/10.22323/1.137.0006>.
- [53] Technical Design Report for the ATLAS Inner Tracker Strip Detector. Technical Report CERN-LHCC-2017-005. ATLAS-TDR-025, CERN, Geneva, Apr 2017. URL <https://cds.cern.ch/record/2257755>.
- [54] The ATLAS TRT collaboration, E Abat, T N Addy, et al. The ATLAS Transition Radiation Tracker (TRT) proportional drift tube: design and performance. *Journal of Instrumentation*, 3(02):P02013, feb 2008. URL <http://dx.doi.org/10.1088/1748-0221/3/02/p02013>.
- [55] A Vogel. ATLAS Transition Radiation Tracker (TRT): Straw Tube Gaseous Detectors at High Rates. Technical Report ATL-INDET-PROC-2013-005, CERN, Geneva, Apr 2013. URL <https://cds.cern.ch/record/1537991>.
- [56] Joao Pequeno. Computer Generated image of the ATLAS calorimeter, Mar 2008. URL <https://cds.cern.ch/record/1095927>.
- [57] *ATLAS liquid-argon calorimeter: Technical Design Report*. Technical design report. ATLAS. CERN, Geneva, 1996. URL <https://cds.cern.ch/record/331061>.
- [58] Carolina Gabaldón and the Atlas LAr Collaboration. Electronic calibration of the ATLAS LAr calorimeter and commissioning with cosmic muon signals. *Journal of Physics: Conference Series*, 160:012050, apr 2009. URL <http://dx.doi.org/10.1088/1742-6596/160/1/012050>.
- [59] *ATLAS tile calorimeter: Technical Design Report*. Technical design report. ATLAS. CERN, Geneva, 1996. URL <https://cds.cern.ch/record/331062>.
- [60] *ATLAS muon spectrometer: Technical Design Report*. Technical design report. ATLAS. CERN, Geneva, 1997. URL <https://cds.cern.ch/record/331068>.

- [61] F. Bauer, U. Bratzler, H. Dietl, et al. Construction and test of MDT chambers for the ATLAS muon spectrometer. *Nuclear Instruments and Methods in Physics Research Section A: Accelerators, Spectrometers, Detectors and Associated Equipment*, 461(1-3):17–20, Apr 2001. URL [http://dx.doi.org/10.1016/S0168-9002\(00\)01156-6](http://dx.doi.org/10.1016/S0168-9002(00)01156-6).
- [62] A Aloisio, V Bocci, G Carlino, et al. The RPC Level-1 Muon Trigger of the ATLAS Experiment at the LHC. Technical Report ATL-DAQ-CONF-2006-004. ATL-COM-DAQ-2006-011, CERN, Geneva, Mar 2006. URL <http://dx.doi.org/10.1109/RTC.2005.1547462>.
- [63] T. Argyropoulos, K. A. Assamagan, B. H. Benedict, et al. Cathode Strip Chambers in ATLAS: Installation, Commissioning and in Situ Performance. *IEEE Transactions on Nuclear Science*, 56(3):1568, 2009. URL <http://dx.doi.org/10.1109/TNS.2009.2020861>.
- [64] S. Majewski, G. Charpak, A. Breskin, et al. A thin multiwire chamber operating in the high multiplication mode. *Nuclear Instruments and Methods in Physics Research*, 217(1):265, 1983. URL [http://dx.doi.org/https://doi.org/10.1016/0167-5087\(83\)90146-1](http://dx.doi.org/https://doi.org/10.1016/0167-5087(83)90146-1).
- [65] Fabio Sauli. Principles of operation of multiwire proportional and drift chambers. 92 p. CERN, CERN, Geneva, 1977. CERN, Geneva, 1975 - 1976, URL <http://dx.doi.org/10.5170/CERN-1977-009>.
- [66] E. Etzion, Y. Benhammou, J. Ginzburg, et al. The certification of ATLAS thin gap chambers produced in Israel and China. *IEEE Symposium Conference Record Nuclear Science 2004*. URL <http://dx.doi.org/10.1109/nssmic.2004.1462188>.
- [67] Georges Aad, Brad Abbott, Jalal Abdallah, et al. (ATLAS Collaboration). Performance of the ATLAS muon trigger in pp collisions at $\sqrt{s}=8$ TeV. Performance of the ATLAS muon trigger in pp collisions at $\sqrt{s}=8$ TeV. *Eur. Phys. J. C*, C75(CERN-PH-EP-2014-154. CERN-PH-EP-2014-154):120. 19 p, Aug 2014. 19 pages plus author list (34 pages total), 17 figures, 3 tables, submitted to European Physics Journal C, All figures including auxiliary figures are available at <http://atlas.web.cern.ch/Atlas/GROUPS/PHYSICS/PAPERS/TRIG-2012-03>, URL <http://dx.doi.org/10.1140/epjc/s10052-015-3325-9>.
- [68] M. Aharrouche and ATLAS Electromagnetic Barrel Calorimeter Collaboration. Energy Linearity and Resolution of the ATLAS Electromagnetic Barrel Calorimeter in an Electron Test-Beam. 2006. [arXiv:physics/0608012](https://arxiv.org/abs/physics/0608012), URL <http://dx.doi.org/10.1016/j.nima.2006.07.053>.
- [69] P. Adragna et al. Testbeam studies of production modules of the ATLAS tile calorimeter. *Nucl. Instrum. Meth.*, A606:362, 2009. URL <http://dx.doi.org/10.1016/j.nima.2009.04.009>.

Thesis plan

November 2019 - January 2020: Framework Development and Validation

The multiple frameworks in the Z+hf analysis group currently show promise, but are not yet ready for full analysis. During this time period, it would be ideal to achieve the following goals:

- Implement systematic uncertainties. Currently the ZHFReader code has functionality for the systematics, but they do not function correctly
- Validate between the frameworks. This requires participation within the analysis groups and it not fully attainable by working alone, however there are some steps that could already be taken to build on the progress made during the "coding days @ CERN" event

February 2020 - April 2020: Production of top and multijet enriched control regions

Measurement of prevalent backgrounds can be performed in order to reduce uncertainties before unfolding, or even to avoid propagating negligible backgrounds through the entire analysis. During this time period, it would be ideal to achieve the following goals:

- Create a multijet enriched control region to enrich multijet event numbers by deliberately requiring the presence of multijet background events (for example by required two same sign muons as opposed to two opposite sign muons)
- Create a top control region to enrich top event numbers by treating emu events as a signal source as opposed to ee or mumu events
- Analyse these control regions and their systematic uncertainties in order to obtain accurate event numbers and neglecting to propagate these backgrounds through the analysis if these backgrounds are negligible

May 2020 - July 2020: Flavour fit

In the same way that top and multijet control regions can be used to perform accurate measurements of these backgrounds, a flavour fit can be used to distinguish between the Z + light, Z + charm, and Z + bottom backgrounds. This is especially important for the Z+b process, as z + light and Z + charm are two of the largest background contributors. During this time period, it would be ideal to achieve the following goal:

- Perform an accurate flavour fit for both the Z+b and Z+bb channels
- Investigate the expected fraction of Z+bb events in the Z+b selection and if it would be worthwhile to make an alternate Z+b selection to reduce this fraction

August 2020 - October 2020: Unfolding and generator comparisons

Unfolding is the crucial step that allows an analysis taking place at detector level to be transposed to particle level in order to obtain meaningful results. Prior to unfolding, the best possible modelling of the obtained data can be found by performing comparisons between multiple varieties of Monte Carlo generator. More MC samples from a greater variety of generators can be obtained by making the analysis appealing to PMG members. During this time period, it would be ideal to achieve the following goals

- Reproduce existing work using a variety of different MC generators, such as with the inclusion of MadGraph samples
- Unfold the analysis to a high degree of accuracy using tools developed by the analysis group during the "coding days @ CERN" event